sustainability

MDPI

Article

Synthesis and Characterization of a Wood Biomass Ash-Derived Multipurpose Sustainable Lightweight Geopolymer: A Pilot Study in Wastewater Treatment

Ina Pundienė [1,*], Jolanta Pranckevičienė [1], Aušra Mažeikienė [2], Yiying Du [1], Kinga Korniejenko [3], Vygantas Bagočius [4] and Ernestas Ivanauskas [5]

[1] Laboratory of Concrete Technologies, Institute of Building Materials, Vilnius Gediminas Technical University, Sauletekio av. 11, LT-10223 Vilnius, Lithuania; jolanta.pranckeviciene@vilniustech.lt (J.P.); yiying.du@vilniustech.lt (Y.D.)
[2] Research Institute of Environmental Protection, Vilnius Gediminas Technical University, Sauletekio av. 11, LT-10223 Vilnius, Lithuania; ausra.mazeikiene@vilniustech.lt
[3] Faculty of Materials Engineering and Physics, Cracow University of Technology, 31-155 Cracow, Poland; kinga.korniejenko@pk.edu.pl
[4] Department of Marine Engineering, Faculty of Marine Technology and Natural Sciences, Klaipeda University, H. Manto str. 84, LT-92294 Klaipeda, Lithuania; vygantas.bagocius@ku.lt
[5] Faculty of Civil Engineering and Architecture, Kaunas University of Technology, Studentų str. 48, LT-51367 Kaunas, Lithuania; ernestas.ivanauskas@ktu.lt
* Correspondence: ina.pundiene@vilniustech.lt

Abstract

This work supports the circular economy and sustainable material by facilitating the creation of low-carbon materials with enhanced elimination of nutrients from wastewater, thereby assisting in preventing eutrophication. Porous geopolymers, owing to their distinctive pore structure and numerous superior properties, including noise reduction and thermal insulation, have a wide range of potential applications in the building sector, chemical industry, and water treatment. Developing low-carbon-footprint porous geopolymer materials is an important step toward creating multipurpose lightweight materials that can serve as structural materials and, at the same time, as adsorbents. In this study, it was revealed that the porous material created during the hydrothermal synthesis of (lime–Portland cement-based aerated composition), by replacement of sand with wood biomass bottom ash (WBA), can be used as porous aggregates (PA) for adsorbent development. PA was produced with an apparent porosity of 65%, a density of 610 kg/m^3, and a compressive strength of 2.0 MPa. The effectiveness of employing an air-entraining additive (AEA) and creating PA in geopolymers was tested. A different-molarity activator was used, and wood biomass fly ash (WFA) and metakaolin (MK) waste were used as precursors for the synthesis of porous geopolymers. Using an air-entraining admixture in geopolymers allows for the production of lightweight geopolymers with densities up to 1400 kg/m^3, compressive strengths up to 8.0 Mpa, and apparent porosities up to 38.4%. Such properties, together with their low cost, offer good prospects for geopolymers in the construction industry. By utilizing PA in the geopolymer composition, a lightweight geopolymer (GPA) with a density of 985 kg/m^3 and a compressive strength of 3.9 Mpa, with 42.0% apparent porosity, was obtained. The materials effectively removed phosphorus from biologically treated wastewater: PA had an efficiency of up to 82.5%, the geopolymer with AEA had an efficiency of up to 88.4%, and GPA had an efficiency of up to 97%. The created GPA enhances the adsorbent's sorption capacity, resulting in extremely high phosphorus uptake efficiency.

Academic Editor: Muhammad Junaid Munir

Received: 3 January 2026
Revised: 3 February 2026
Accepted: 10 February 2026
Published: 21 February 2026

Keywords: wood biomass ash; geopolymer; waste valorization; circular economy; sustainable wastewater treatment; phosphorus removal; porosity

1. Introduction

Recent comprehensive evaluations have reinforced the appeal of geopolymer materials as environmentally friendly construction materials. Porous geopolymers are an attractive option for thermal insulation due to their favorable mechanical and physical characteristics. As synthesis occurs through foaming at reduced temperatures and low energy usage, their CO_2 emissions are reduced. Because of its distinctive pore structure and numerous superior qualities, including noise reduction and thermal insulation, porous geopolymer has several potential uses in the building, chemical, and water treatment industries [1]. Therefore, it is crucial to synthesize porous geopolymers employing ash and slag as raw materials.

Water pollution is a significant worldwide environmental problem. However, the quality of water is deteriorating mainly due to mineral extraction and overuse of synthetic fertilizers in farming. Phosphorus is released into aquatic environments by a range of human activities, including quarrying, commercial and agricultural processes, and rock weathering. When water's phosphate content exceeds 0.02 mg/L [2], it causes eutrophication, which lowers dissolved oxygen levels, hinders the growth of aquatic organisms, and may even pose a significant health risk to humans [3]. Phosphorus is a major water contaminant that contributes to the eutrophication of freshwater habitats [4].

Water quality may decrease due to eutrophication, caused by excessive phosphorus release into surface waters. Phosphorus removal is becoming increasingly necessary as phosphorus pollution of water increases. High levels of phosphorus and other contaminants cause algae to grow rapidly, which diminishes the water's light and oxygen content, leading to "death zones" [5]. Phosphorus's detrimental effects on the ecosystem can be greatly reduced by wastewater treatment and phosphorus collection [6]. Therefore, it Is crucial and necessary to recycle and reuse phosphorus from wastewater. Preventing eutrophication greatly depends on the development of inexpensive, highly effective phosphate adsorbents [7,8].

The primary technique for recovering phosphorus from wastewater is adsorption [9]. Because of its high degree of versatility, it is considered among the more attractive technologies for eliminating phosphorus [10,11]. The anions' affinity for the material's surface, the corresponding quantity, and the pH all affect the extent of adsorption. As an effective method for eliminating anions, anion exchange has drawn attention [8]. The main benefit of naturally occurring adsorbents is their affordability. However, their usefulness is limited by their varied characteristics and often low efficiency, which is frequently less than 5 mg/g [4]. Bentonite has shown a low phosphorus adsorption capacity of 0.3 mg/g, while kaolinite has a slightly higher capacity of 0.32 mg/g [12,13]. A variety of adsorbents, including dolomite [14], mussel shells [15,16], and sludge [17], were tested for their phosphate adsorption capacity. Despite the successful removal of phosphates, these adsorbents are not widely used in practice because of their high cost (resin) or difficulty in separating from the aqueous phase (red mud or bentonite fine particles) [18].

Among synthetic adsorbents, geopolymers are known for their remarkable adsorption properties for heavy metals and organic–inorganic contaminants, such as dyes, ammonium, radionuclides, surfactants, antibiotics, CO_2, and more [19–22]. The ability of geopolymer to completely or partially substitute other cations present in aqueous environments for alkali metal ions within its structure is a noteworthy feature. Furthermore, the geopolymer structure is inherently microporous and mesoporous. Because of its crystal-like architecture,

composed of circular molecular bonds, geopolymer is the perfect, inexpensive adsorbent for wastewater [3,8,23]. Geopolymers are amorphous aluminosilicates formed from silicate and aluminum silicate precursors such as fly ash, slag, kaolin, and industrial waste [24,25]. With an optimal removal rate of 85%, the tailored geopolymers prepared with varying ratios of sodium hydroxide, binder, fly ash, and nanoparticles exhibited effective phosphate removal from the liquid [26]. The crystalline structure of fly ash can be optimized, and the features of geopolymers further improved by partially substituting metakaolin [27]. The physical characteristics of geopolymers can be improved [28] and also improved [27] by preparing fly ash and metakaolin mixes. Pretreatment of BFA plays a significant role in improving its adaptability in geopolymers. The application of milled BFA in geopolymer systems, together with metakaolin as an aluminosilicate source, increases the compressive strength of the material from 14 to 40 mPa, compared with only 7.5 to 28 mPa when unmilled BFA is used. The SiO_2/Al_2O_3 ratio in the system plays an important role. If too small or too large, this ratio does not ensure mechanical properties. The most promising results are reached when SiO_2/Al_2O_3 ratios vary in the range of 8–16 [29–31].

A promising new class of environmentally benign binders for removing heavy metals, contaminants, and chemical compounds from wastewater is geopolymers made from various types of fly ash. Using wood biomass ash in geopolymers has been shown to reduce the potential leaching of heavy metals and to enhance their sorption properties [32]. High-CaO fly ash and biomass ash can be employed as raw materials to create geopolymer/zeolite-P materials with SiO_2/Al_2O_3 molar ratios of 6.0 and 8.0. Geopolymerization is followed by a hydrothermal treatment at 100 °C for zeolitization. The presence of zeolite-P in geopolymers essentially increases the material's sorption properties [24,33,34].

Although fly ash may yield intriguing outcomes, it can introduce unwanted ions into the aquatic environment [4]. Porous geopolymers are produced via physical and chemical foaming techniques and exhibit a large number of internal pores [1]. Because of their huge surface area, porous geopolymers offer more active binding sites for the sorption of heavy metals [3].

Foaming of geopolymers can be achieved through both physical and chemical methods [1,26]. Foaming in the physical method is caused by high water evaporation. Water in the activator solution rapidly reaches high temperatures, evaporates quickly, and creates foam within the mass [35]. The most straightforward and popular technique for foaming geopolymer materials is chemical foaming, also known as direct foaming [36]. Direct foaming typically involves a reaction in which various foaming agents and an alkaline medium are used to initiate pore formation during geopolymerization [37]. To initiate pore formation during geopolymerization, direct foaming typically involves a reaction with multiple foaming compounds and an alkaline medium.

Using this method, blowing agents are introduced into the slurry, resulting in a foamed slurry via either direct gas injection or mechanical frothing. The porosity structure and characteristics of the final material can be controlled by choosing the foaming agent and its amount in the geopolymer paste [37–39]. It is possible to generate high porosity up to about 63 vol%; the structure consists of intrinsic micro- and mesopores [40]. When different foaming additives are used, a porous structure is formed through chemical reactions that produce gaseous products, such as oxygen or hydrogen [41]. Hydrogen peroxide, silicon, zinc, and aluminum powders, along with sodium hypochlorite and sodium perborate, are recognized foaming agents for the synthesis of porous zeolite/geopolymer materials [42].

Commonly used foaming agents include H_2O_2 [43,44] and metal powders, such as Si [45] and Al [46,47]. In addition, sodium peroxide (Na_2O_2) [48] and sodium hypochlorite (NaOCl) may also be used as chemical pore-forming agents [49]. However, most foamed geopolymers have a low mechanical strength (up to 2.5 MPa), which makes their use as

adsorbents difficult [50]. This is why creating balanced geopolymers is an essential task for most researchers. Another major drawback in the production of such geopolymers is the lack, compared to OPC, of established design codes, due to the variable chemical composition of the used precursors.

By combining hydrogen peroxide, fly ash, metakaolin, and an alkaline solution, a porous zeolite/geopolymers adsorbent was developed that successfully removed lead from wastewater. According to the data, the absorption efficiency of lead increases with the porosity of the geopolymers [23,51]. Nickel (II), arsenic (III), and antimony (III) removal amounts are increased more by blast-furnace slag added to porous geopolymers than by aluminosilicate geopolymers, rising from 0.331 to 4.421 mg/g, 0.179 to 0.52 mg/g, and 0.06 to 0.34 mg/g, respectively [52].

By adding the organic surfactant cetyltrimethylammonium bromide (CTAB) and H_2O_2 to the CTAB solution, a series of three distinct porous geopolymers was synthesized [53]. The mesoporous geopolymer produced using both CTAB and H_2O_2 showed a notable improvement compared to the geopolymer synthesized without any chemical agents. While the geopolymer produced without additives exhibited a specific surface area of 79 m^2/g and a porosity of 0.087 cm^3/g, the resulting mesoporous geopolymer prepared with both CTAB and H_2O_2 achieved a particular pore area of 126 m^2/g and an evenly distributed pore volume of 0.138 cm^3/g.

Geopolymers tested for phosphate removal through adsorption–desorption and regeneration demonstrated the highest porosity (57.2–83.2 vol%), the highest ratio of open to total porosity (66.2–90.8%), and the highest compressive strength (3.4–10.1 MPa). The adsorption capacity of the produced RO/GP structure reached 92.4 mg-P/g. [49]. Porous geopolymers exhibit varying removal capabilities due to their high specific surface area and varying porosity.

To assess phosphate adsorption capacity and examine its mechanism, metakaolin and fly ash were used as base materials in the literature [3,8]. The removal effectiveness of phosphate adsorption in wastewater using 0.8M activator was, on average, 30.33% greater than using 1.2M activator. As a result, the fly ash and metakaolin mix, activated with 0.8 M activator, had the highest phosphate adsorption capacity of 35.98 mg/kg and the highest removal efficiency of 94.21% in wastewater. In the mineral phase of a fly ash–metakaolin blend, new zeolite forms were created that could aid in the adsorption of phosphate by geopolymers. The findings showed that surface complexation, ligand exchange, and electrostatic gravitation were the underlying mechanisms of phosphate adsorption.

For improved sorption properties, designed aggregates are often used. The use of porous aggregate is promising. Among known porous aggregate calcium silicate hydrates, reticulated porous CSH has a sorption capacity of 152 mg/g, depending on production technology and Ca/Si ratio [54]. Clay-mineral-based aggregate has a sorption capacity of 0.491 mg/g [55]. Porous calcium–silicate–hydrate composite [56–58] showed remarkable adsorption up to 130 mg/g. The synthesis conditions for calcium silicate hydrates, including CaO/SiO_2 ratio, water-to-solid ratio, and isothermal conditions for processing, ensure the desired properties and environmental friendliness. The molar ratio of CaO to SiO_2, crystallinity, and other variables affect the ability of calcium silicate hydrates to adsorb phosphorus [56].

Recently, different waste materials have been increasingly used for the synthesis of calcium silicate. For example, biofuel bottom ash can be used as a component in synthesis, replacing natural sand and helping conserve environmental assets. The viability of substituting bottom ash from solid waste combustion for quartz sand in the design of autoclaved aerated concrete (AAC) was examined, as noted in Ref. [59]. The density and compressive strength of AAC increase with the fineness of bottom ash. The reactive silica

content of bottom ash may affect the formation of tobermorite crystals and, consequently, their sorption characteristics.

Therefore, novel, affordable, and efficient adsorbents still need to be developed to address the issues listed above. Thus, the purpose of this work is, first, to create a porous geopolymer suitable for the construction sector and, second, to create various adsorbents (foamed and porous geopolymers by combining porous aggregates with geopolymers), assess their adsorption properties, and compare their effectiveness. Prior investigations have examined geopolymers' ability to adsorb various contaminants, demonstrating their potential as an adsorbent for treating wastewater and restoring the environment. The optimal preparation conditions for achieving the highest phosphate removal effectiveness remain unknown, as does the impact of geopolymers made by combining these two materials on phosphate adsorption in water.

In light of the aforementioned explanations, the goals of this study are to use fly ash and metakaolin as precursors to synthesize geopolymers and to investigate the impact of the modulus of the alkali activator on the adsorption properties of the geopolymers. On the grounds of the hypothesis that a lower modulus improves sorption properties and influences the highest phosphate removal efficiency in water, the potential adsorption mechanism of phosphate is considered.

2. Materials and Methods

2.1. Untreated Ingredients

2.1.1. Raw Materials

Pine sawdust processing bottom ash (WBA) and wood biomass fly ash (WFA) were collected by the Ekobaze Waste Management in Vilnius, Lithuania from the energy power plant by burning pine sawdust and chips. Before employment, WBA and WFA were milled for 8 h to produce smooth particles, and the particle size distributions are presented in Figures 1a and 2a. In the WBA morphologies shown in Figure 1b, the coarse particles display irregular, heterogeneous shapes with rough surfaces. Most likely, these particles are quartz, calcite, or wollastonite. Between coarser particles, smaller particles may belong to portlandite, quartz, calcite, wollastonite, and unburnt wood residues. In the morphologies of WFA in Figure 2b, it can be seen that the WFA particles are much smaller than the WBA particles. Coarser particles belong to quartz, calcite, lime aggregates, and unburnt wood residues. Predominantly, small particles may belong to portlandite, quartz, calcite, and small unburnt wood residues.

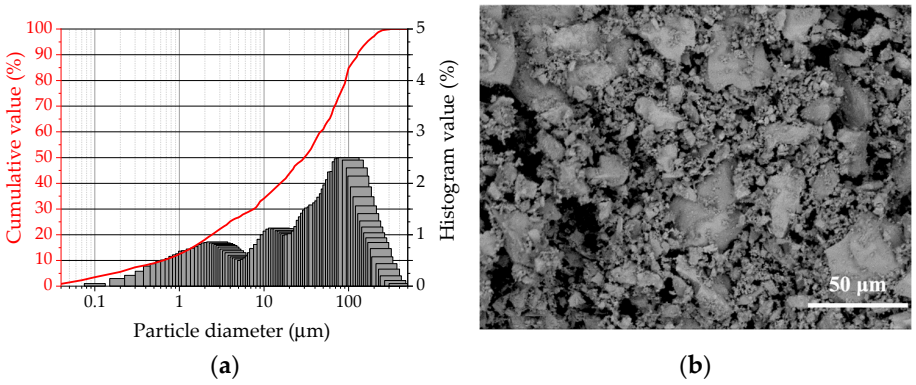

Figure 1. WBA: (**a**) particle size distribution and (**b**) SEM image of particle morphology.

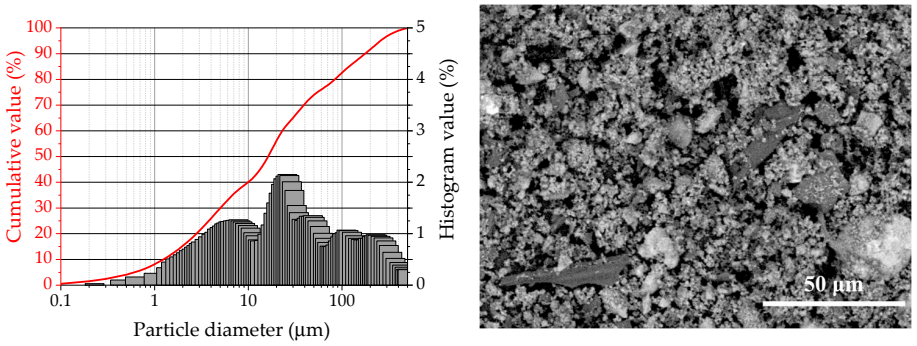

Figure 2. WFA: (**a**) particle size distribution and (**b**) SEM image of particle morphology.

In the X-ray diffraction (XRD) patterns of the WBA shown in Figure 3a, quartz was the main crystalline phase. In addition, calcite, portlandite, and wollastonite were also identified. In the X-ray diffraction (XRD) patterns of the WFA shown in Figure 3b, quartz, lime, and dicalcium silicate were the main crystalline phases; calcite and portlandite were also observed. In the morphologies of WFA in Figure 2b, it can be seen that the WFA particles are much smaller than the WBA particles. Coarser particles belong to quartz, calcite, lime aggregates, and unburnt wood residues. Predominantly, small particles may belong to portlandite, quartz, calcite, and small unburnt wood residues.

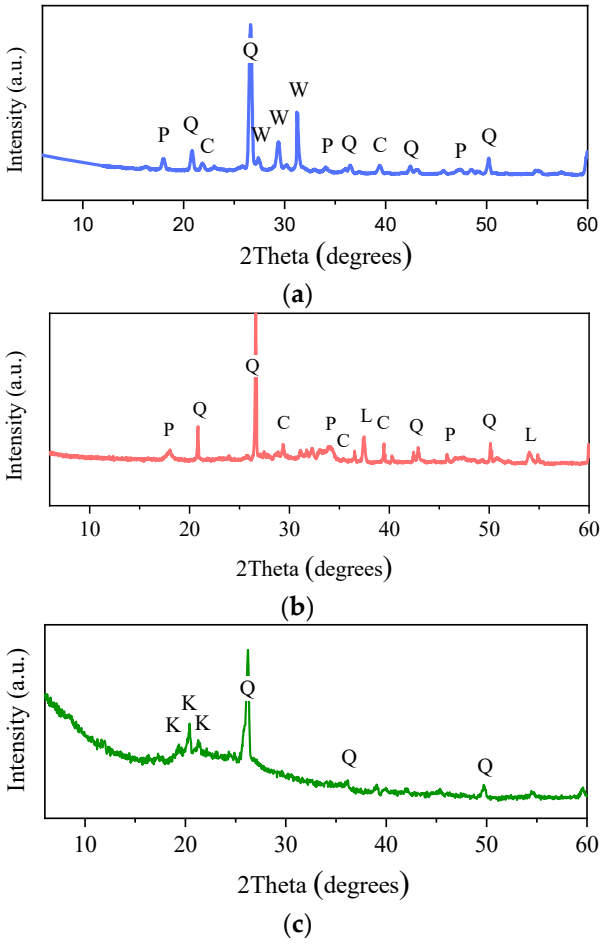

Figure 3. *Cont.*

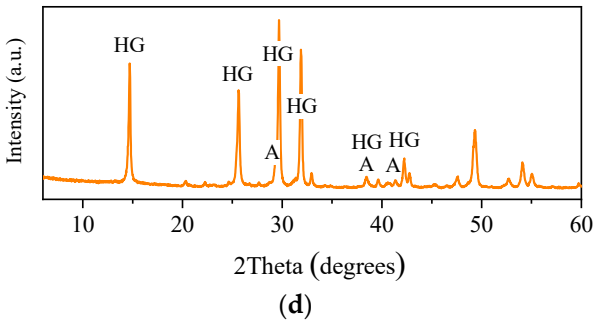

(**d**)

Figure 3. XRD patterns of raw materials: (**a**) WBA; (**b**) WFA; (**c**) MK; (**d**) gypsum. Mineral phases identified: Q—quartz, P—portlandite, C—calcite, W—wollastonite, L—lime, K—kaolinite, HG—hemihydrate gypsum, A—anhydrite.

The aluminum silicate employed in this research on geopolymer synthesis was obtained from metakaolin (MK) (Stikloporas Ltd., Vilnius, Lithuania). The MK was produced at 820–850 °C during the foamy glass granule production. Particle size distribution of MK is presented in Figure 4a. MK particles vary in dimension from 1.2 µm to 19.7 µm and are flake-like in form (Figure 4b).

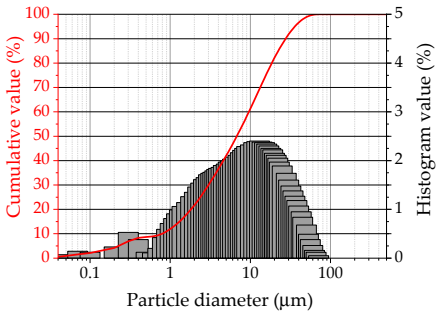

(**a**)

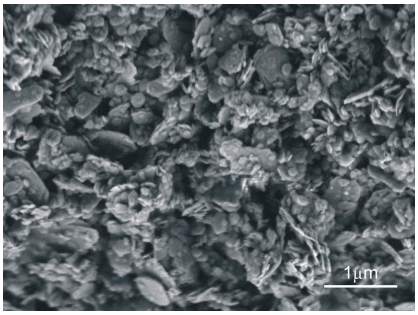

(**b**)

Figure 4. MK: (**a**) particle size distribution and (**b**) SEM image of particle morphology.

In the provided X-ray diffractogram of the used MK (Figure 3c), the most intense crystalline phase was quartz, and a wide range of amorphous phases was observed at 20–30 theta. The existence of the non-crystalline phase confirms the presence of amorphous SiO_2 and Al_2O_3.

In this study, Portland cement CEM I 42.5 R (PC), as per EN 197-1:2011, was used. The initial and final setting times were 142 and 186 min. The compressive strengths after 7 and 28 days were 29.9 MPa and 55.6 MPa, respectively. Particle size distribution is presented in Figure 5.

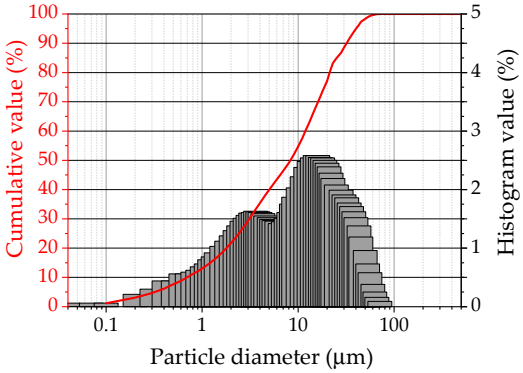

Figure 5. The distribution of PC particles by size.

Gypsum was used for the production of autoclaved aerated materials. The content of $CaSO_4 \cdot 2H_2O$ in the gypsum (Dolina Nidy Sp. z o.o., Pinczow, Poland) was 89.97%. The particle size distribution is presented in Figure 6a. Figure 6b presents an SEM image of the gypsum particles. The image shows that the gypsum consists of irregularly shaped, angular, and plate-like (lamellar) particles that tend to form agglomerates. The particle surfaces are rough and uneven, with visible microcracks and surface irregularities, typical of crystalline $CaSO_4 \cdot 2H_2O$. This morphology indicates a relatively high specific surface area, which is beneficial for reactivity in binder systems and may significantly influence hydration processes and pore structure formation in autoclaved or alkali-activated materials.

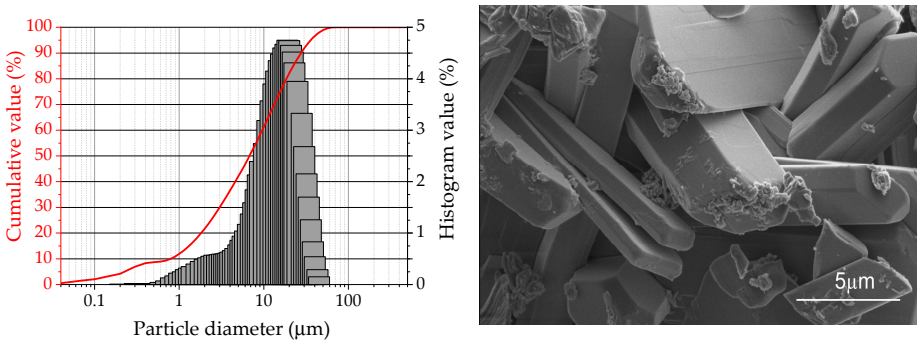

(**a**) (**b**)

Figure 6. Gypsum: (**a**) particle size distribution and (**b**) SEM image of particle morphology.

The properties of WBA and WFA, MK, PC, and gypsum, including their specific surface area, bulk density after processing, and main particle size diameter (d50), are presented in Table 1. The main chemical compositions (in mass%) are presented in Table 2.

Table 1. Particle characteristics.

	Specific Surface Area, m^2/kg	Bulk Density, g/cm^3	Particle Size, µm
WBA	978	1.03	14.43
WFA	835	0.57	11.83
MK	903	0.35	8.63
Gypsum	446	2.32	9.6

Table 2. Chemical composition of materials, %.

	SiO_2	Al_2O_3	Fe_2O_3	CaO	MgO	K_2O	Na_2O	Other
WBA	50.25	9.20	1.90	19.99	6.44	5.71	1.19	4.76
WFA	28.8	2.93	2.22	33.60	5.89	5.86	1.90	18.8
MK	46.1	37.2	1.10	0.20	0.20	0.20	0.50	14.5
PC	20.76	6.12	3.37	62.01	3.19	1.00	0.30	3.25

Based on particle size distribution data, the fineness of the raw materials varies significantly. The coarsest are Al particles; wood biomass bottom ash has a smaller particle size; and the smallest are metakaolin particles. Near metakaolin are Portland cement and gypsum particles. The fineness of metakaolin significantly influences the rate of geopolymerization and product formation.

2.1.2. Activators

Commercially available sodium hydroxide (SH) was used to ensure the geopolymerization reactions. Tianye Chemicals produces SH flakes. The purity of NaOH flakes was (99% min). The density of sodium metasilicate solution (SM), which was made up of 50% sodium silicate (SS) by mass, was 1382 kg/m^3. In the Na_2SiO_3 solution, the SiO_2 and Na_2O molar ratio was 3.2.

2.1.3. Quicklime

Quicklime, a chemical substance, is widely used across various sectors. It is produced by calcining limestone in a furnace at elevated temperatures until it transforms into a whitish powder. Quicklime, which contains more than 70% of active CaO and MgO, is best suited for autoclaved aerated materials. The white quicklime powder containing more than 70% CaO was obtained from Lerochem (Klaipeda, Lithuania).

2.1.4. Alumina Powder

The aluminum powder (Benda-Lutz, Poland, grade 5-6380/80) had an average particle size of 24.40 µm. The aluminum suspension was prepared in a mixer by stirring aluminum powder with a predetermined amount of water at 20 °C.

2.1.5. Air-Entraining Agent

"UFFAPORE TCO", an air-entraining agent (AEA), is a white powder made from sodium alkenes' sulfonate. It ensures that the cement mix forms tiny air gaps. The producer recommends 0.015–0.07% AEA in the paste, based on the OPC amount. It was reported in [60,61] that 0.02% of OPC mass is the optimal amount of AEA for testing (to prevent loss of strength).

2.1.6. Wastewater for Filtration

Wastewater for the studies was collected from small (flow rate up to 5 m^3) individual wastewater treatment plants (WTPs). Samples of treated wastewater were collected from the WTP outlet pipe, and their temperatures were measured on site.

Nitrite nitrogen (NO_2-N), ammonium nitrogen (NH_4-N), nitrate nitrogen (NO_3-N), ortho-phosphate phosphorus (PO_4-P), suspended solids (SS), chemical oxygen demand (COD), biochemical oxygen demand (BOD_7), and other characteristics, such as their pHs, were tested after the samples had been allowed to settle.

Standard analytical techniques [62–69] were employed to establish these indicators' readings.

The average measurements of the three tests conducted on every specimen are shown (Table 3).

Table 3. Qualitative indicators of wastewater, average values.

t, °C	pH	COD, mg/L	BOD_7, mg/L	SS, mg/L	NO_3-N, mg/L	NO_2-N, mg/L	NH_4-N, mg/L	PO_4-P, mg/L
18 ± 2	7.7 ± 0.15	23.0 ± 10	3.5 ± 1.5	4.2 ± 2.5	25.09 ± 6.3	0.36 ± 0.05	6.22 ± 2.5	7.3 ± 2

2.2. Methods of Testing

2.2.1. Particle Size Distribution

Particle size distribution was completed on a Cilas 1090 LD (Orleans, France) particle size analyzer within the diameter range of 0.01–500 µm.

2.2.2. Physical-Mechanical Properties

Formula (1) was used to determine the specimen's apparent porosity P_0:

$$P_0 = \frac{W_m - \rho_m}{\rho_w} \quad (1)$$

where W_m is the water absorption of samples by mass, ρ_m is the density of samples in the dry state, and ρ_w is the density of water.

Mercury intrusion porosimetry (MIP) using the Pore Master PM33-12 (Quantachrome Instruments, Boynton Beach, FL, USA) equipment was used to examine the samples' pore size distributions after 28 days of curing at room temperature. The test sample was collected from the interior layer.

At 20 ± 2 °C and 60 ± 10% relative humidity, the samples' mechanical and physical characteristics were assessed.

Density was calculated with an accuracy of ±5 kg/m^3 in accordance with [70]. The samples' compressive strength was evaluated in accordance with [71].

2.2.3. XRD Analysis

X-ray diffraction (XRD) patterns of the powdered specimens were obtained on a SmartLab X-ray diffractometer (Rigaku, Tokyo, Japan) over a 2θ range of 10–60° to determine the mineralogical phases of the raw materials and manufactured specimens. HighScore 3.0 software (PANalytical B.V., Almelo, The Netherlands) was used to identify the mineralogical phases. The tests were carried out using the Bragg–Brentano geometry with a graphite monochromator on the diffracted beam. The step-scan mode had a step size of 0.02° (in 2θ) and a 1 s per step counting time.

2.2.4. SEM Analysis

The microstructure of the raw materials and samples of various mixes was assessed using the SEM EVO 50 EP (Carl Zeiss, SMTAG, Oberkochen, Germany, resolution 1.5 nm).

2.2.5. Wastewater Treatment

A laboratory bench (Figure 7) was used for wastewater research. The tested material samples were placed in the filtration columns. The stand consisted of two 4.5 cm diameter columns with valves at the bottom. The surface area of one filtration column was 0.00159 m^2.

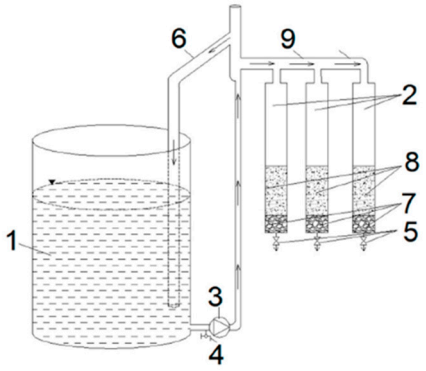

Figure 7. Principal scheme for bench: 1—wastewater tank, 2—filtration columns, 3—wastewater supply pump, 4—wastewater sampling point (before filtration), 5—filtrate collection point, 6—overflow tube, 7—retaining layer, 8—filter media, 9—wastewater distribution pipe to columns.

A pump was applied to supply three filters with transported wastewater at a rate of 0.68 m/h (discharge of 0.96 L/h). Three filters were provided with delivered effluent at a

rate of 0.68 m/h (discharge of 0.96 L/h) using a pump. To evaluate pH and PO_4-P, as well as NO_2-N and NH_4-N concentrations, filtration specimens were collected every 30 min. Column packings (occupied a volume of 250 mL). The sorbent fillers used in the tests were 20–22 cm high, whereas the columns were 60 cm tall. The material fraction (0.5–1.25 mm) and the grain volume (250 mL) were poured into a filtration column (diameter 45 mm) on a supporting layer of pebbles. Wastewater was fed into the columns so that the fillers remained submerged at all times, and filtration occurred from the top down.

2.3. Paste Design and Sample Preparation

2.3.1. Porous Aggregate Preparation

The porous aggregate (PA) was based mainly on cement, quicklime, and gypsum. They were used as calcareous materials. WBA and WFA were used for 2 purposes: as calcareous materials and as a source of silicon oxides. The PA preparation method was as follows: First, water and WBA were poured into the laboratory mixer and mixed. Later, the other ingredients, such as OPC, quicklime, and gypsum, were added, and everything was mixed well at 40 rpm for 3 min. The last step was to add the aluminum powder suspension. Aluminum paste (aluminum paste to water ratio 1:20) was added to water at 20 °C and homogenized by mixing for 5 min to achieve even particle distribution and mass swelling. Since the mass swells during hardening, it was filled to about 2/3 of the autoclave's capacity [72]. The ambient temperature was kept at 25 °C or higher, and the mass swelled and attained its initial strength. The mass swelling lasted about 30–40 min. As the binding material hydrated, the molding mixture gained plastic strength, which was sufficient to prevent the mass from collapsing while also preventing the porous structure from collapsing. After this, the autoclave started the curing process. At this stage, the products were only heated. During the autoclave hardening process, the sample was heated to 65–100 °C for 4 h. It took 1.5 h to reach 65 °C, and over 2.5 h the temperature increased from 65 to 100 °C. After 4 h had passed, heating in saturated water vapor was initiated. The autoclave temperature reached 185 °C over the next 4 h. During this time, the pressure was increased to 1.3 MPa. The sample was kept at 185 °C and 1.3 MPa for 9 h. Then, the samples were cooled to 30 °C for 24 h under reduced pressure. The cooled samples were removed from the molds (measuring 70 mm × 70 mm × 70 mm) and dried to constant weight at 105 ± 5 °C. After this, the physical–mechanical properties were tested. After testing, samples were crushed and sieved through sieves to collect the fraction (0.5–1.25 mm). Table 4 displays the composition of the created aggregate (WBA).

Table 4. The mixing composition of WBA in g.

Composition of PA, g						Oxide Ratio		
WBA	**OPC**	**Quicklime**	**Alumina Paste**	**Gypsum**	**Water**	**Al_2O_3/CaO**	**Al_2O_3/SiO_2**	**SiO_2/Al_2O_3**
67.0	15.0	15.0	0.14	2.86	78.8	0.049	0.098	10.53

2.3.2. Alkaline Activator Solutions Preparation

Different concentrations of alkaline activator solutions (ACS) were produced by diluting the alkaline activator with distilled water in the amounts required for testing with 6M, 5M, and 4M NaOH solutions. A modified activator was a sodium metasilicate solution (dry-matter mass ratio 3/1) combined with a 6M, 5M, and 4M NaOH solution. ACS was prepared by mixing all components for 60 min with a magnetic mixer. The pH of the activators used ranged from 13.35 to 13.2.

2.3.3. Fresh Alkali-Activated Material

Preparation with AEA

The mix design presented in Table 5 was used to make fresh alkali-activated material (AAM) pastes. The total water amount in the compositions was stable. All raw materials were stored at ambient temperature for 24 h before treatment. The mixing process was performed at 20 ± 1 °C. The dry-mixed WFA and MK components were combined with the ACS, and the paste was stirred for three minutes at 140 rpm. AEA was dissolved in 1/3 of the required water, then mixed for 30 s by hand mixer at 40 rpm. Then, the remaining water was added to the AEA solution, and the mixture was immediately mixed for 60 s with a hand mixer at 40 rpm. After this time elapsed, the prepared foamed AEA was poured into the paste, and mixing was continued for 3 min at 40 rpm. Next, samples measuring 70 mm × 70 mm× 70 mm were filled with the paste and vibrated for 5 s. The samples were heated in a preheated oven at 80 °C for 24 h, then cooled and tested. After testing, samples were crushed and sieved through sieves to collect the fraction (0.5–1.25 mm).

Table 5. The mixing composition of AAM in g.

	Components, g						Oxide Ratio			
AAM	**WFA**	**MK**	**NaOH**	**Na_2SiO_3**	**Total Water Content**	**AEA**	**Al_2O_3/Na_2O**	**Al_2O_3/CaO**	**Al_2O_3/SiO_2**	**SiO_2/Al_2O_3**
G6	20.0	80.0	24.0	8.00	170.0	0.01	1.10	17.2	0.66	1.51
G5	20.0	80.0	20.0	6.65	170.0	0.01	1.47	1.72	0.68	1.46
G4	20.0	80.0	16.0	5.30	170.0	0.01	1.84	17.2	0.69	1.41

Preparation with PA

Fresh AAM paste, named GPA, was prepared from the created PAs according to the mix design in Table 6. All used raw materials were maintained at an ambient temperature for 24 h before testing. Using a mixer, the dry materials were combined for 3 min at 30 rpm, then for 5 more minutes at 40 rpm. The ACS was added to the dry mixture, and the paste was mixed for 3 min at 40 rpm using a mixer. Next, samples measuring 70 mm × 70 mm× 70 mm were filled with the paste and vibrated for 5 s. The samples were heated in a preheated oven at 80 °C for 24 h, then cooled and tested. After testing, samples were crushed and sieved through sieves to collect the fraction (0.5–1.25 mm).

Table 6. The mixing composition GPA (AAM with PA) in g.

	Components in g					Oxide Ratio			
WFA	**PA**	**MK**	**NaOH**	**Na_2SiO_3**	**Total Water Content**	**Al_2O_3/SiO_2**	**Al_2O_3/Na_2O**	**Al_2O_3/CaO**	**SiO_2/Al_2O_3**
60.0	30.0	10.0	16.0	5.30	210.0	0.21	0.23	0.15	4.75

3. Results

3.1. The Density of PA, Foamed Geopolymers, and Porous Geopolymers

Autoclaved aerated concrete (AAC) has an open-cell structure with air pores. Only high-density AAC, more than 550 kg/m^3, can possess pore distances large enough for a closed-cell structure of air pores to be formed [73]. The density of autoclaved aerated concrete typically ranges from 500 to 650 kg/m^3 [1,74,75]. The density of the created PA is 610 kg/m^3 (Figure 8). The curing process is important for determining the properties and the structure formation. The strength and structural characteristics of AAM pastes are significantly impacted by the curing process. As noted in the literature [76], curing at temperatures ranging from 40–50 °C to 80–85 °C for 4–48 h is one of the essential requirements for the sintering of alkali-activated materials. For G6 samples prepared with 6M ACS, the density is 1410 kg/m^3; for G4 samples prepared with 4M ACS, the density

is 1360 kg/m^3 (Figure 8). The lower molarity in the mixtures results in a lower sample density [53,77]. As expected, the density of the GPA sample with porous PAs is lower than that of the G6 and G4 compositions and reaches 985 kg/m^3.

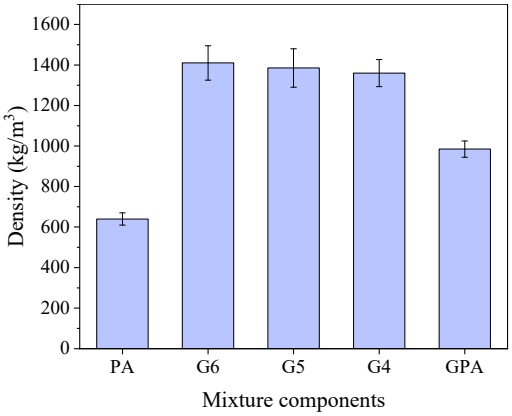

Figure 8. The density of the samples, depending on the ACS molarity.

3.2. Apparent Porosity

An apparent porosity test of the samples confirmed the density test results (Figure 9). With a PA density of 610 kg/m^3, the apparent porosity was 65.21%. As noted in the literature [73], the pore volume in AAC products ranges from 64.5% to 91%. Depending on the density of autoclaved aerated concrete (600–700 kg/m^3), air pores occupied 50–60% of the samples. The apparent porosity also depends significantly on the density [1]. As noted in this research, H_2O_2-foamed geopolymers exhibit apparent porosities of 69.6%, 84.6%, and 86.5% for samples with densities of 708 kg/m^3, 359 kg/m^3, and 210 kg/m^3, respectively. In the case of geopolymers, some trends are observed. A decrease in the molarity of ACS leads to lower viscosity [78] and, consequently, a greater ability to retain more air bubbles in its structure during mixing. Higher ACS molarity in the composition results in higher density and lower apparent porosity in the samples. Molarity is the primary factor influencing the density and apparent porosity of geopolymers after curing and aging, according to research. Water serves as a solvent during the dissolution and rearrangement of aluminosilicate precursors to form a geopolymer; it does not enter the geopolymer framework. The development of pores was initiated by water removal during the setting process [79]. There may also be interactions between chemical compounds and the precursor that can affect the air void structure of geopolymer, including submicron pores in the range of 0.1–10 μm [80,81].

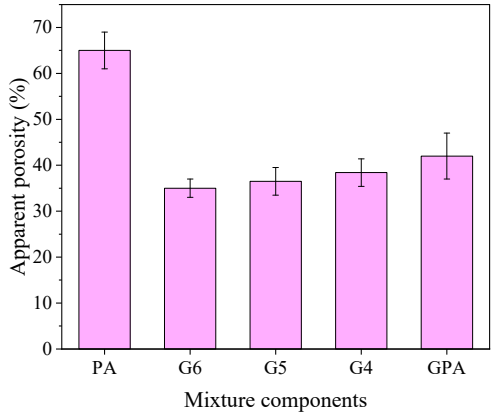

Figure 9. Apparent porosity of samples.

3.3. The Samples' Pore Structure and Microstructure

The presented images (Figure 10a,b) of the pore size distribution and microstructure of the specimens essentially confirm the apparent porosity results. In the PA sample, the most significant proportions of pores are those with diameters of 0.01–0.1 μm (28.5%) and 60–350 μm (45%). A smaller proportion of pores (approximately 26%) have diameters larger than 0.3 mm. The pore size distribution is multimodal, with an average pore size of 53 μm. The sample microstructure is presented in Figure 10b. Tobermorite is the primary phase in the aerated autoclaved products produced. Numerous studies [54,59,82,83] have shown that adding waste materials or industrial by-products to aerated autoclaved products can alter reaction outcomes. The inclusion of WBA promotes the development of tobermorite. The morphology of tobermorite is greatly impacted by the substitution of WBA for quartz sand, which aids in the creation of tobermorite. As reported in the research [82], increasing the amount of WBA caused plate-like tobermorite to replace needle-like tobermorite in the control sample. In our case, both forms of tobermorite are evident in the sample. Additionally, some unreacted WBA particles are visible on the surface.

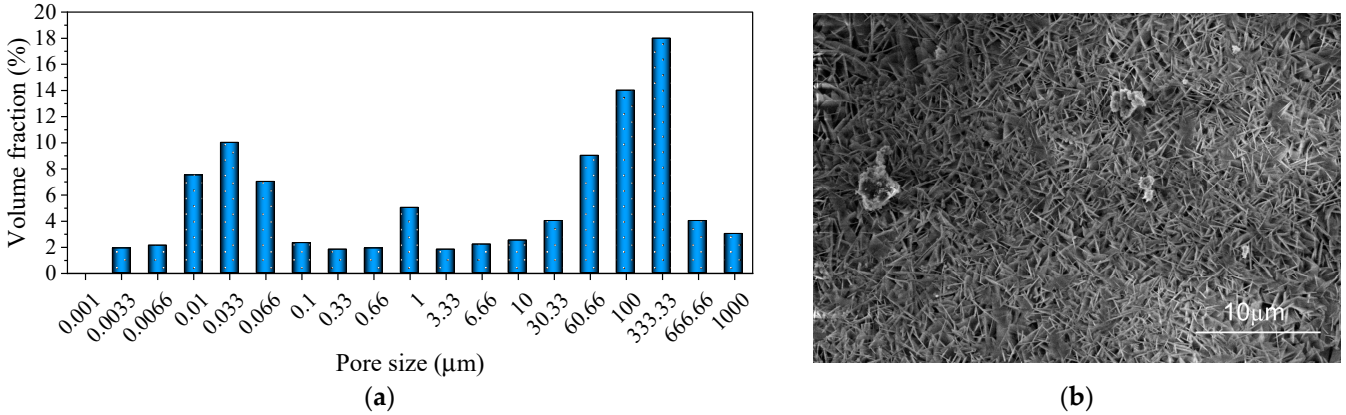

(**a**) (**b**)

Figure 10. Sample PA: (**a**) pore structure and (**b**) microstructure.

In the ACS, the molarity was 6 M, and the observed pore distribution in the samples was uneven. In the sample, pores with sizes from 0.003 to 0.03 accounted for 20% of the total (Figure 11a,b). In the PA sample, such a size was not detected, particularly in the G6 structure-dominated pores (0.1 to 3.5 μm; 48%), which were absent. Additionally, the amount of pores with a size of 60 to 100 μm was 10%, and the amount of pores with a size larger than 0.3 mm decreased to 13%. Higher ACS molarity leads to faster geopolymer gel formation [1,84], resulting in smaller pores. The average pore size was 2.2 μm. The sample structure was compact and dense, consisting of a gel phase, some unreacted particles, and several pores in the matrix. The same observations are presented in the literature [85].

The distribution of pores in sample G4 was less consistent across volumes (Figure 12a). The overall number of smaller pores (0.003 to 0.07 μm) was 27% higher than in the G6 sample. In the structure, pores with a size of 0.3 to 3.5 μm (39%) dominated. The pores with sizes 10 to 300 μm occupied (15.7%) and pores with sizes larger than 300 μm occupied (14.1%), which was caused by less viscous paste and the entrainment of larger air bubbles in the paste during mixing. The average pore size was 3.4 μm. The structure of the sample was less compact than the G6 sample structure. The same gel phase and some unreacted particles were observed. Many small pores existed in the sample structure. Such pores most likely formed during sample synthesis, as water vapor escaped from the sample structure [86].

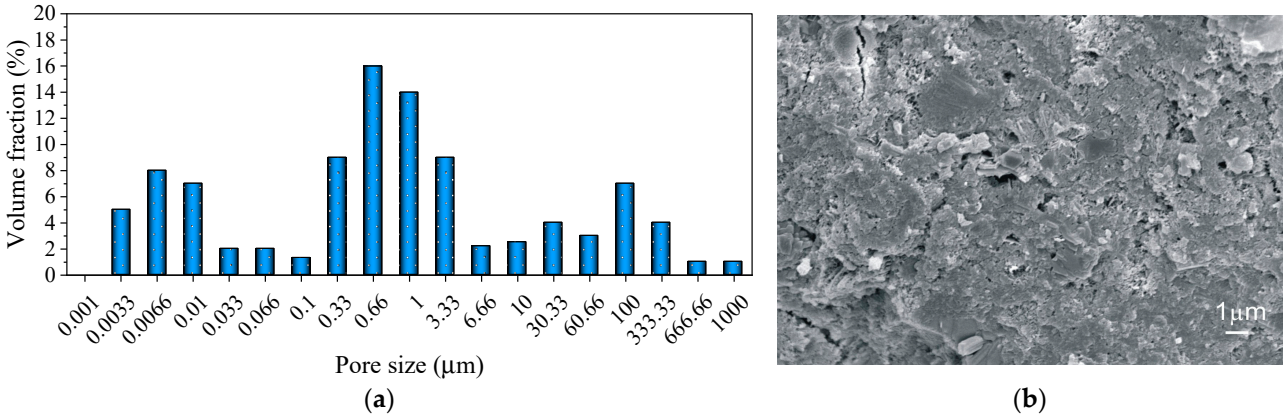

Figure 11. Sample G6: (**a**) pore structure and (**b**) microstructure.

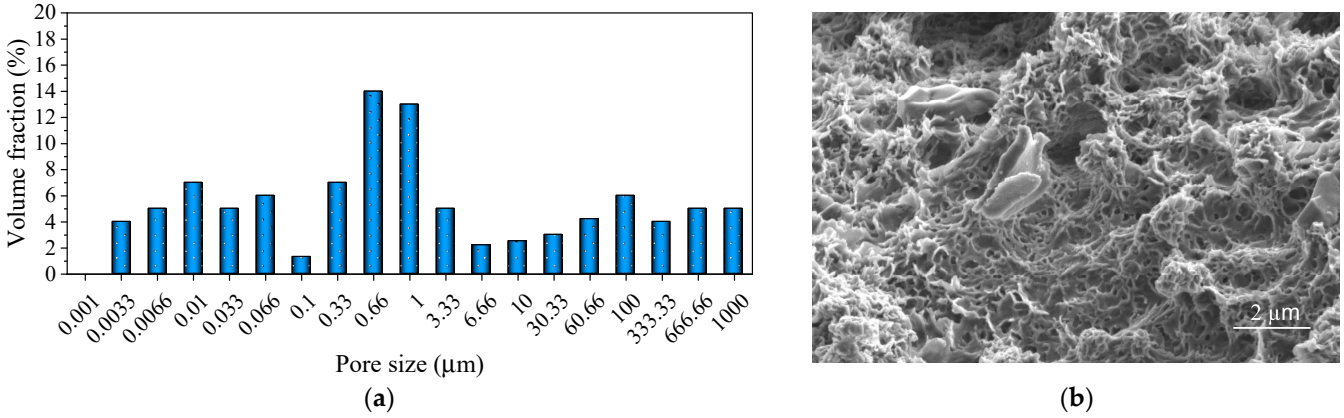

Figure 12. Sample G4: (**a**) pore structure and (**b**) microstructure.

The sample GPA structure presented with three main pore size distributions. The first peak belonged to pores with sizes 0.003 to 0.07 μm, accounting for 14% (Figure 13). The second had pores 0.3 to 3.5 μm in size, accounting for 29%. The third peak was observed in pores 30–330 μm, accounting for 36%. The average pore size was 20.6 μm. The sample structure was not compact, consisting of a gel phase and plate-like tobermorite [87]. However, different pore sizes were present in the sample structure, which can form during both component mixing and the synthesis process due to water evaporation.

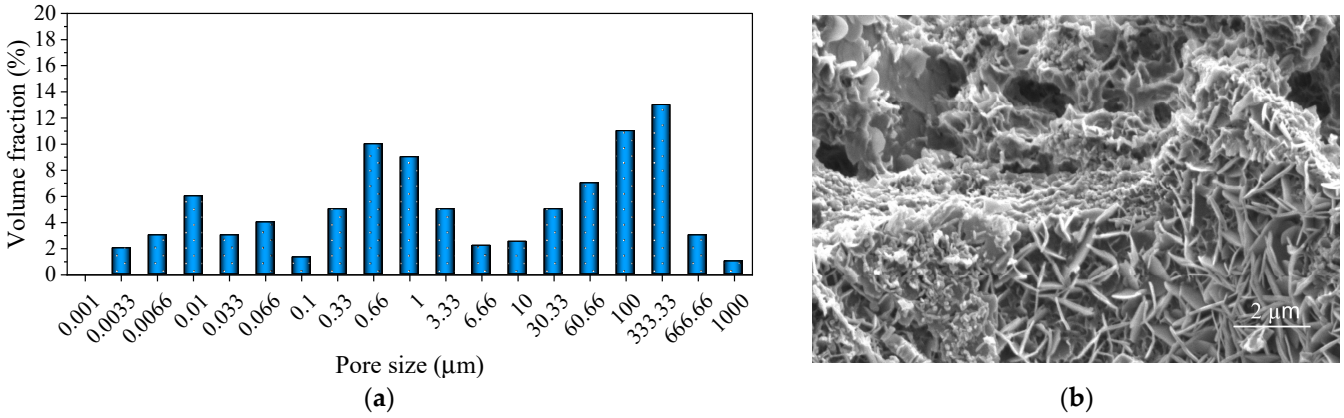

Figure 13. Sample GPA: (**a**) pore structure and (**b**) microstructure.

3.4. Mechanical Properties

Porosity, water absorption, and mechanical strength are related. The sample PA compressive strength was 2.04 MPa. According to one study [87], autoclaved aerated

concrete with fly ash replacing quartz sand can have a compressive strength of 2–2.5 MPa. The pozzolanic activity of fly ash increases the tobermorite formation in autoclaved aerated concrete. The bulk density of foamed geopolymers is critical and strongly correlated to the compressive strength [41]. The mechanical properties of geopolymers were determined after curing at 80 °C and aging for 28 days. During the production of foamed geopolymers, the bulk density is mainly controlled by the gas-foaming rate and the specific gravity of the constituent materials [88]. The specific gravity of the component substances and the gas-foaming speed are the primary factors influencing the bulk density throughout the manufacturing of foamed geopolymers.

We can see that higher ACS concentrations in the pastes result in higher compressive strengths in the specimens after 28 days (Figure 14). Such tendencies are also concluded in [83]. When foamed geopolymers are 505 kg/m^3, the compressive strength reaches 1.6 MPa [41]. For 1100 kg/m^3, the compressive strength is 2.9 MPa; for higher densities (1300–1500 kg/m^3), it is 3.6–4.2 MPa. According to research [89], higher NaOH molarity results in higher compressive strength than lower molarity. The compressive strength data on the 28th day showed the biggest growth, reaching 10%. The samples' compressive strength drops by 19% as the molarity of ACS drops. The literature [90,91] confirms similar findings, demonstrating that AAM strength increases with increasing ACS molarity. An increase in the Na/Al ratio in metakaolin-based AAM can accelerate polymerization and increase the compressive and flexural strengths of the samples, as reported by Ref. [92].

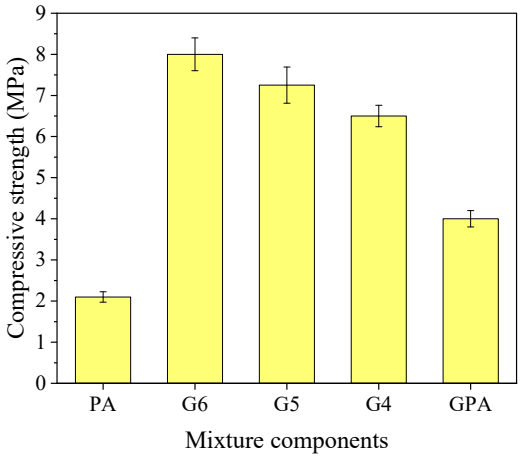

Figure 14. Mechanical property changes in the samples, depending on composition.

A higher concentration of NaOH in a solution reduces insoluble metakaolin residues and improves the compressive strength of the prepared AAM specimens [93]. In GPA samples, the addition of lower-density PAs reduces compressive strength by up to 38% compared to G4 samples. However, this value is sufficiently high and can ensure the mechanical strength of adsorbents [1].

We can see that mechanical properties correlate with porosity and structure development research, which shows that lower ACS increases porosity and decreases compressive strength. The porous geopolymers prepared using ACS at different molarities exhibit strengths ranging from 8 to 6.5 MPa. Such properties enable the use of the porous geopolymers created to serve as structural, lightweight components in building enclosures.

The employment of PA in geopolymers enables the manufacture of materials with sufficiently high strength up to 4 MPa, but not sufficient for construction needs. Thus, the use of this type of geopolymer as an adsorbent is promising.

3.5. XRD Test

The mineral composition of the PA sample was evaluated using XRD analysis (Figure 15). According to test results, the PA is mostly composed of 1.13 nm tobermorite, quartz, and dicalcium silicate. The basic reaction in aerated concrete is CaO from quicklime reacting with silica to form 1.13 nm tobermorite. It is known that the minerals of the tobermorite group determine the mechanical properties of aerated concrete [94]. The WBA, which is mainly quartz, also participates in the formation of tobermorite [59]. As reported in the research, replacing quartz sand with bottom ash increased tobermorite formation.

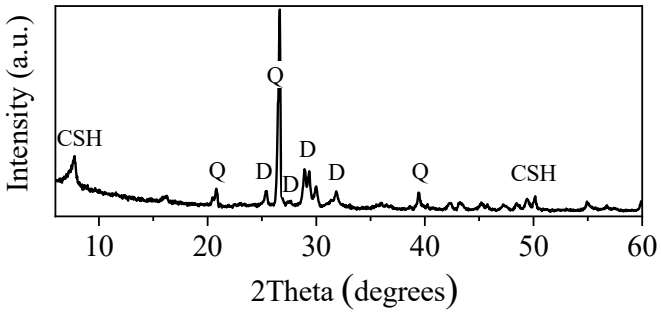

Figure 15. PA sample XRD analysis (CSH: tobermorite, Q: quartz, D: dicalcium silicate).

The mineral composition of specimens G6 and G4 with 6M and 4M ACS was evaluated by XRD analysis after storing at 80 °C (Figure 16). According to XRD data, both G6 and G4 samples include the same crystalline phases: quartz (SiO_2), which appeared from raw metakaolin [95], N-A-S-H, which appeared while metakaolin was being activated, and hydroxide sodalite ($1.08Na_2O{\cdot}Al_2O_3{\cdot}1.68SiO_2{\cdot}1.8H_2O$), which belongs to the sodalite group of zeolites. Higher ACS molarity in the samples resulted in higher hydroxide sodalite crystallization rates, which are by-products of the geopolymerization reaction. The hydroxide sodalite diffraction peak intensities in G6 samples are higher than in the G4 samples. Additionally, the quartz diffraction peak intensity is noticeably lower in the G6 samples than in the G4 samples. N-A-S-H formation during the alkali activation process is characterized by a shift to higher degrees of halo at 10–30 2Theta (degrees), indicating an amorphous phase in the raw materials [96,97]. These investigations support the findings of the compressive strength test and show that a larger ACS molarity in the mixes can have a substantial impact on mineral creation and, in turn, the samples' mechanical and physical characteristics.

3.6. Sorption Test

Figure 17 presents the results of research into the removal of phosphate from wastewater using various adsorbents. The quantity of phosphate elimination was almost 97% at a phosphate loading of 7.3 mg/L on GPA, while it reached just 82.5% for PA during the first hour.

It is challenging to remove phosphorus from less-polluted wastewater. For example, a coagulant for phosphorus removal from municipal wastewater reduced phosphate loading from 34 mg/L to 1.98 mg/L after 1 h of testing. In our case, there is an opportunity to reduce the phosphate loading from 7.3 mg/L to 0.2 mg/L over the same test duration [98]. As reported in the literature [99], phosphate adsorption by biofuel fly ash increased rapidly at the onset of sorption and reached saturation within 2 h. The explanation of this behavior is as follows: in the composition of biofuel fly ash, alkali oxides, such as K_2O and Na_2O, are readily dissolved and raise the solution's pH throughout the adsorption process [100,101]. It is believed that the rise in pH that results from the dissolution of these oxides improves the adsorption of phosphate by biofuel fly ash [102].

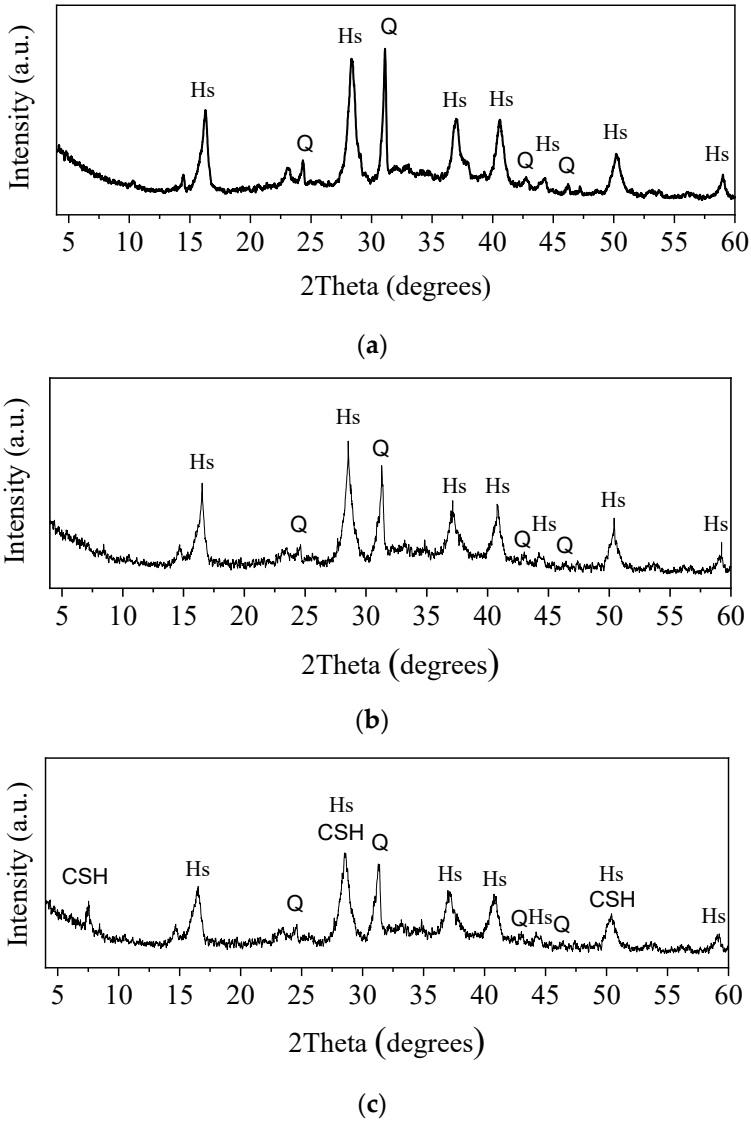

Figure 16. XRD analysis of samples: (**a**)—G4, (**b**)—G6, and (**c**)—GPA (Hs—hydroxide sodalite, Q—quartz, CSH—tobermorite).

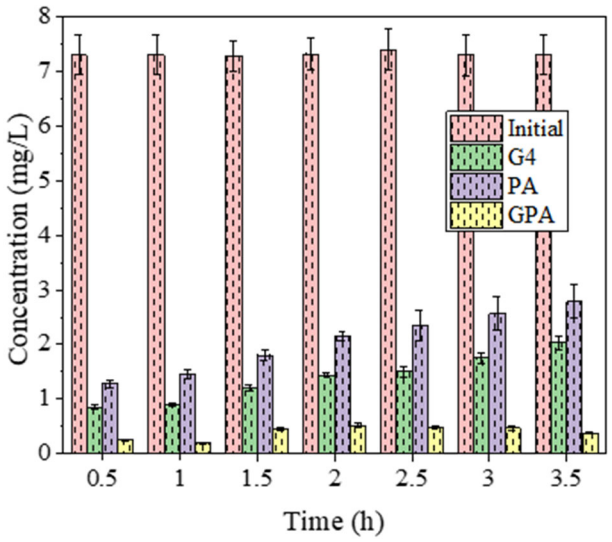

Figure 17. PO_4 sorption in different composition samples.

In our case, all adsorbents increased the pH of the filtered wastewater from 7.7 to 8.7. According to the Lithuanian Republic Wastewater Management Regulation, wastewater may be discharged into the natural environment only when its pH is within the range of 6.5–8.5. However, this applies to regular (frequent) discharges, i.e., when more than 10% of the total wastewater volume is discharged within one hour. Instantaneous pH values in the range of 8.4–10 are permitted when the discharge duration within one hour does not exceed 6 min. When tertiary treatment (using the sorbents investigated in this study) is applied in individual treatment units, the Regulation's requirements would be met. Compared with a commercial phosphorus retention sorbent (Filtralite P), our investigated sorbents exhibited higher phosphorus removal efficiency, while pH remained similar [103].

For the G4 adsorbent, phosphate removal was 88.4%. The produced geopolymers, consisting of fly ash and metakaolin, show adsorption efficiencies of 20–30% over 2 h, increasing to 30–50% over 3–4 h [49,104]. Zeolites show greater effectiveness in phosphorus removal, as modified natural zeolites achieved the same efficiency (62–85%) in phosphate removal [105]. It is evident that phosphate removal rates are fast, and equilibrium is reached in 3–3.5 h for all adsorbents.

In summary, all materials effectively removed phosphorus from phosphates in biologically treated wastewater: G4 efficiency ranged from 88.4 to 72.2%, PA from 82.5 to 61.8%, and GPA from 93 to 97%.

Standard water treatment techniques, such as flocculation and coagulation, struggle to remove nitrate, a stable, highly soluble ion. The most popular technique for eliminating nitrate from water is ion exchange. In order to exchange nitrate ions for chloride ions until the resin is depleted, nitrate-loaded water is passed through a bed of strong-base anion-exchange resins. The highest nitrate retention capacity (13.01 mg/g) was achieved using Relite A490 resin [106].

The removal of NO_3 from wastewater using the aforementioned adsorbents is shown in Figure 18. The NO_3 removal with the tested adsorbents is much lower than that for phosphorus removal. For the GPA adsorbent, NO_3 removal was 16.7% at NO_3 loadings of 24 mg/L, and for the PA, it was less than 0.01% during the first hour. For the G4 adsorbent, NO_3 removal was 10.8% at the same time. It is evident that the NO_3 removal rate is slow, and equilibrium is reached in 2 h for all adsorbents. As reported in the literature [107], NO_3 removal is a complex process. In the best adsorbent composition (enriched zeolite), a removal of total nitrogen of 10.91 ± 4.23 mg N/L was achieved.

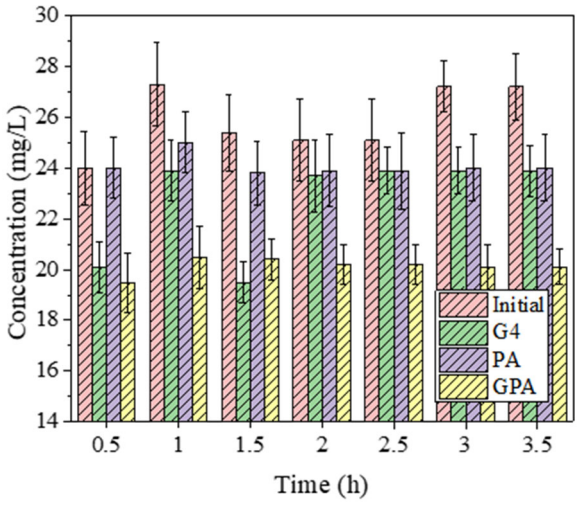

Figure 18. NO_3 sorption in different composition samples.

Another study [108,109] shows that using biological carriers carried into the carbon-limited anoxic zone reduced NO_3 emissions from 5.20 ± 2.71 to 0.82 ± 0.37 g-N/(m^3·d).

Generally, it can be concluded that nitrate nitrogen removal from the tested wastewater was insignificant, and the efficiency of the used adsorbents was low (Figure 18). It is concluded that none of the tested adsorbents reduced nitrate concentrations in filtered wastewater. There may be several reasons for this. As noted in the literature [110], higher Si/Al ratios (above 2) decrease the concentration of negatively charged aluminate sites ($[AlO^4]^-$) available for anion exchange, thereby lowering NO_3^- sorption capacity via surface complexation. Anions such as nitrate and nitrite may form coordination bonds or electrostatic interactions with hydroxyl groups on the surface (e.g., -Al-OH and -Si-OH). Increasing porosity positively affects diffusion by reducing the number of Al sites, which are crucial for binding anions such as nitrate [111].

On the other hand, as the filtration columns operate for a longer period, bacteria accumulate in their fillings, forming a film. Bacteria accumulate in the columns from filtered wastewater, i.e., the activated sludge microorganisms remaining after biological treatment. Since the column fillings are submerged, the bacteria carry out nitrate respiration (denitrification); thus, the concentrations of nitrate nitrogen (NO_3-N) and nitrite nitrogen (NO_2-N) in the filtered wastewater decrease.

The removal of NH_4-N from wastewater using the aforementioned adsorbents is shown in Figure 19. The amount of NH_4-N removal was almost 96.1% at an NH_4-N loading of 6.22 mg/L on GPA after 0.5 h. For both, PA and G4 removal was 92.9% during the first 0.5 h. Particularly in high-porosity materials, nitrogen species physically diffuse into the geopolymer's pores and become trapped. In our case, GPA samples exhibit higher porosity and a greater abundance of 10–300 μm pores, which can lead to higher adsorption properties.

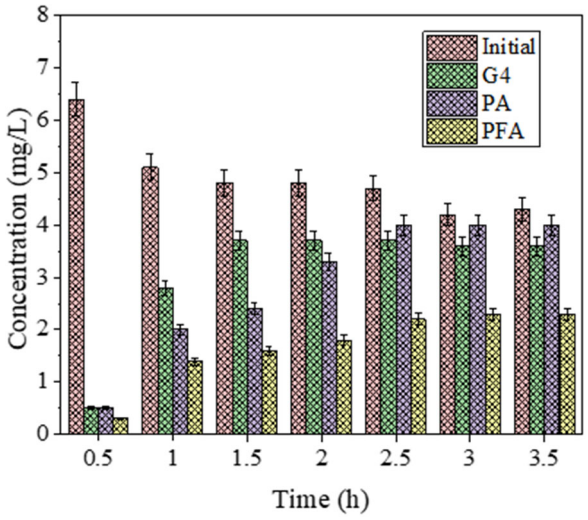

Figure 19. NH_4 sorption in different composition samples.

Research has shown that by introducing the flow electrode after 60 min of procedure, the elimination of NH_4^+ for synthetic zeolite, NaCl-zeolite, and EDTA-2Na-based zeolite was achieved >80%, although the elimination of Na^+ was approximately twenty percent (23.84%, 20.2%, and 22.64%) [112]. EDTA-2Na is an exceptional Na salt, and the EDTA anion may form a complex with metal cations [112,113]. Zeolites treated with EDTA-2Na have been the subject of numerous previous investigations. Through ion exchange with exchangeable cations like Ca^{2+} in the zeolite, it was discovered that the protonated N atoms in EDTA improve the adsorption of EDTA on the zeolite surface [114]. Additionally, by

extracting Al from zeolite while preserving crystallinity, EDTA anions can create additional pores. Pristine Na-P1 zeolite has an ion-exchange capability of 470 meq NH_4^+/100 g [115].

In addition, alkali concentration significantly affects ion-exchange capacity values. The greatest ion-exchange capacity requires an alkali activator quantity of 15% [116]. Over the next 3 h, the initial wastewater NH_4-N concentration decreased from 6.22 to 4.3 mg/L. The main decrease in the initial wastewater NH_4-N concentration occurred after 2 h, when it dropped to 4.6 mg/L. All three tested adsorbents removed ammonium nitrogen from wastewater for a while (2 h), with GPA effectiveness of 59%, PA effectiveness of 26.1%, and G4 effectiveness of 13%.

This behavior can be attributed to the rapid occupation of easily accessible surface and near-surface adsorption sites during the initial stage, followed by partial desorption and re-equilibration of ammonium ions as the system approached adsorption–desorption equilibrium. Additionally, the limited availability of high-affinity sites and competition effects within the pore structure may contribute to the observed decrease in apparent removal efficiency over time. During 3.5 h of filtration, the NH_4-N concentration in the filtrates of columns filled with G4 and PA changed slightly. GPA turned out to be a more effective adsorbent for removing ammonium nitrogen from water: after 3 h of filtration, its NH_4-N retention efficiency was 40%.

The presence of the created zeolitic hydroxide sodalite structure also enhances sorption properties. Geopolymers act like zeolites, adsorbing NH_4^+ via ion exchange: the negatively charged AlO_4/SiO_4 framework captures the positively charged ammonium ions, which are balanced by alkali cations from the activator. According to the literature, lower Si/Al ratios, as in cases G6, G5, and G4 (1.51, 1.46, 1.41), should lead to more AlO_4 tetrahedra, resulting in a higher negative charge density and, consequently, more cation-exchange sites for NH_4^+. However, in our case, the most effective adsorption properties are observed for GPA composition with a Si/Al ratio of 4.75, possibly due to a high porous aggregate pore volume and a high specific surface area.

Created zeolites reduce the concentration of NH_4-N in water due to their special crystalline structure, which acts as an ion-exchange sieve, selectively absorbing ammonium ions from water into their pores and replacing them with other ions, such as Na ions. Further study of the produced adsorbents will allow them to be modified in the future to improve their mechanical and durability properties, as well as water absorption and porosity [117].

Given the costs and technological limitations, producing foamed geopolymers poses several challenges. Although the production of geopolymers reduces the CO_2 footprint compared to OPC, they are flexible in the use of waste materials, but they also have drawbacks, such as high curing temperatures, limited design codes, and expensive activators [118–120]. Conventional geopolymer curing often requires high temperatures (60–80 °C), which increases energy costs. However, the practical value of this work lies in the creation of a foamed geopolymer suitable for treating polluted waters. The need for such adsorbents worldwide is great, and the proposed production method is simple and easily replicable. This means that in the future, synthesis can be scaled up and costs will decrease.

There are several ways to regenerate the adsorbent. The adsorbent created, saturated with phosphorus and other compounds, should be regenerated or further used in accordance with the principles of the circular economy. The cleaning process for adsorbents is usually very expensive, as it may require solvent rinsing, heating, electrochemical, ultrasonic, or plasma treatment, which can be selected based on the adsorbent and contaminant properties [121]. The best possible solution is to use the contaminated adsorbent directly without additional treatment. The use of adsorbents in agriculture, as fertilizers, could

be considered. However, such a solution requires extensive additional research, which is planned for the future.

4. Conclusions

1. The study of MK-based foamed geopolymers shows that using an air-entraining admixture and different-molarity ACS allows the creation of lightweight geopolymers with densities of 1360–1400 kg/m^3, compressive strength of 6.5–8.0 MPa, apparent porosity of 35.0–38.4%, and water absorption of 16.9–18.7%.
2. During the geopolymer sintering, the structure develops more quickly in foamed samples with greater ACS molarity in the MK-based geopolymer. Following geopolymer synthesis at 80 °C, the foamed samples' density and compressive strength increased with increasing MK-based geopolymer ACS molarity, whereas apparent porosity decreased.
3. Reducing the ACS molarity and raising the Al_2O_3/Na_2O and Al_2O_3/SiO_2 ratios in the compositions, respectively, results in a nearly 20% decrease in the samples' compressive strength and an increase in apparent porosity due to the development of hydroxide sodalite, a synthesis product. However, decreasing the ACS molarity increases water adsorption. An increased ACS molarity in the composition results in a more intense geopolymerization and the development of a greater amount of reaction product hydroxide sodalite. XRD results validate the compressive strength test results.
4. Compared to sample G4, a higher molarity of ACS in the G6 sample led to the formation of a lower (up to 27%) amount of smaller pores (0.003 to 0.07 μm) and a higher amount (up to 20%) of pores with sizes 0.3 to 3.5 μm and coarser than 10 μm. The greater formation of pores with sizes of 0.3 to 3.5 μm at a lower molarity of the activator (4M) led to its selection for further studies on the development of lightweight composites with a PA.
5. The research conducted for porous material hydrothermal synthesis revealed that WBA can replace the use of sand in the composition without degrading the main properties of the material. Using WBA as the raw material, a porous material with a density of 610 kg/m^3, a compressive strength of 2 MPa, an apparent porosity of 65%, and a water adsorption of 35% was obtained. Pores occupy the most significant percentage of the porous material PA, with diameters ranging from 60 to 350 μm (45%) and higher than 0.3 mm (26%)—pores with diameters ranging from 0.01 to 0.1 μm occupied (28.5%) of PA. Synthesized by hydrothermal treatment, porous material can be used alone and in geopolymer composition for sorption purposes.
6. By utilizing PA as a porous filler in geopolymer composition, a lightweight geopolymer material with a density of 985 kg/m^3, compressive strength of 3.9 MPa, apparent porosity of 42.0%, and water absorption of 33.2% was obtained. The sample GPA structure is presented with three principal pore size distributions. The most significant percentage of pores in the lightweight geopolymer material GPA is occupied by pores with diameters ranging from 30 to 330 μm, accounting for 36%. Pores with a size of 0.3 to 3.5 μm occupied 29%, and pores with a size of 0.003 to 0.07 μm occupied 14%. Due to a significant decrease in the Al_2O_3/CaO ratio to 0.15, Al_2O_3/SiO_2 ratio to 0.21, and Al_2O_3/Na_2O ratio to 0.23 in the GPA composition, the geopolymerization reaction and the formation of the reaction product, are reduced. However, the phase composition of the GPA sample contents includes both a geopolymeric matrix and PA minerals, such as quartz and 1.13 nm tobermorite. The combination of hydroxide sodalite, 1.13 nm tobermorite, and newly formed sodium aluminum silicate hydrate ensures sufficient mechanical properties at a low GPA density.

7. This research demonstrated that porous material synthesized by hydrothermal treatment can be used in geopolymer technology for the development of lightweight adsorbents. In summary, by incorporating AEA and PA into the composition, geopolymers with high phosphorus adsorption capacity were produced. All created materials effectively removed phosphorus from biologically treated wastewater: G4 had an efficiency of 88.4–72.2%, PA had an efficiency of 82.5–61.8%, and GPA had an efficiency of 93–97%. The greater percentage of pores in the 0.3–3.5 μm size range in the G4 sample matrix resulted in better sorption properties in the G4 and GPA samples. The created porous material, PA, improved phosphorus uptake efficiency. The investigation revealed that adsorption duration affects the adsorption capacity for ammonium nitrogen. All three tested adsorbents removed ammonium nitrogen effectively from the wastewater for 2 h, but the adsorption capacity of G4 and PA did not change significantly thereafter. GPA proved to be a more effective adsorbent for removing ammonium nitrogen from wastewater: after 3.5 h of filtration, the retention efficiency was 40%.
8. By encouraging the reuse of industrial by-products, lowering dependency on traditional Portland cement-based materials, and facilitating effective phosphorus removal from treated wastewater, the developed ash-derived lightweight geopolymer adsorbents help achieve sustainability goals while also aiding in eutrophication control and circular nutrient management. By facilitating the removal of nutrients from wastewater and encouraging the reuse of industrial by-products, the suggested strategy supports the UN Sustainable Development Goals (SDGs 6 and 12).

Author Contributions: Conceptualization, I.P., K.K., A.M. and J.P.; methodology, I.P., V.B., A.M. and J.P.; software, Y.D. and E.I.; validation, I.P., J.P. and A.M.; formal analysis, J.P., V.B. and K.K.; investigation, I.P., J.P. and V.B.; resources, V.B. and E.I.; data curation, A.M. and Y.D.; writing—original draft preparation, I.P. and J.P.; writing—review and editing, A.M., K.K., J.P. and I.P.; visualization, Y.D., V.B. and E.I.; supervision, J.P.; project administration, J.P.; funding acquisition, I.P. All authors have read and agreed to the published version of the manuscript.

Funding: This research was funded by the Research Council of Lithuania under the M-ERA.NET 3 Cofund programme (Grant No. S-M-ERA.NET-24-2) and by the Polish National Centre for Research and Development under the M-ERA.NET 3 programme (Grant No. M-ERA.NET3/2023/67/CleanLake/2024), within the project "Development of water treatment systems that counteract the eutrophication process of lakes based on zeolites obtained from industrial by-products".

Institutional Review Board Statement: Not applicable.

Informed Consent Statement: Not applicable.

Data Availability Statement: The original contributions presented in this study are included in the article. Further inquiries can be directed to the corresponding author.

Conflicts of Interest: The authors declare no conflicts of interest.

References

1. Yatsenko, E.A.; Goltsman, B.M.; Izvarin, A.I.; Kurdashov, V.M.; Ryabova, A.V. Influence of foaming additives on the porous structure and properties of lightweight geopolymers based on ash–slag waste. *Constr. Build. Mater.* **2024**, *443*, 137629. [CrossRef]
2. Omwene, P.I.; Kobya, M. Treatment of domestic wastewater phosphate by electrocoagulation using Fe and Al electrodes: A comparative study. *Process Saf. Environ. Prot.* **2018**, *116*, 34–51. [CrossRef]
3. Liang, K.; Wang, X.Q.; Chow, C.L.; Lau, D. A review of geopolymer and its adsorption capacity with molecular insights: A promising adsorbent of heavy metal ions. *J. Environ. Manag.* **2022**, *322*, 116066. [CrossRef]
4. Svedaite, E.; Dambrauskas, T.; Renman, A.; Renman, G.; Baltakys, K. Adsorption kinetics of phosphorus on a calcium silicate hydrate based adsorbent. *Ceram. Int.* **2025**, *51*, 5557–5566. [CrossRef]

5. Devlin, M.; Brodie, J. Nutrients and Eutrophication. In *Marine Pollution—Monitoring, Management and Mitigation*; Reichelt-Brushett, A., Ed.; Springer Nature: Cham, Switzerland, 2023; pp. 75–100. [CrossRef]
6. Nobaharan, K.; Novair, S.B.; Lajayer, B.A.; van Hullebusch, E.D. Phosphorus Removal from Wastewater: The Potential Use of Biochar and the Key Controlling Factors. *Water* **2021**, *13*, 517. [CrossRef]
7. Dodds, W.K.; Smith, V.H. Nitrogen, phosphorus, and eutrophication in streams. *Inland Waters* **2016**, *6*, 155–164. [CrossRef]
8. Zhou, W.; Lan, T.; Shang, G.; Li, J.; Geng, J. Adsorption performance of phosphate in water by mixed precursor base geopolymers. *J. Contam. Hydrol.* **2023**, *255*, 104166. [CrossRef]
9. Yao, S.; Wang, M.; Liu, J.; Tang, S.; Chen, H.; Guo, T.; Yang, G.; Chen, Y. Removal of phosphate from aqueous solution by sewage sludge-based activated carbon loaded with pyrolusite. *J. Water Reuse Desalin.* **2018**, *8*, 192–201. [CrossRef]
10. Zou, Y.; Zhang, R.; Wang, L.; Xue, K.; Chen, J. Strong adsorption of phosphate from aqueous solution by zirconium-loaded Ca-montmorillonite. *Appl. Clay Sci.* **2020**, *192*, 105638. [CrossRef]
11. Lin, J.; Zhan, Y.; Wang, H.; Chu, M.; Wang, C.; He, Y.; Wang, X. Effect of calcium ion on phosphate adsorption onto hydrous zirconium oxide. *Chem. Eng. J.* **2017**, *309*, 118–129. [CrossRef]
12. Gu, S.; Kang, X.; Wang, L.; Lichtfouse, E.; Wang, C. Clay mineral adsorbents for heavy metal removal from wastewater: A review. *Environ. Chem. Lett.* **2018**, *17*, 629–654. [CrossRef]
13. Liu, C.J.; Li, Y.Z.; Luan, Z.K.; Chen, Z.Y.; Zhang, Z.G.; Jia, Z.P. Adsorption removal of phosphate from aqueous solution by active red mud. *J. Environ. Sci.* **2007**, *19*, 1166–1170. [CrossRef]
14. Karaca, S.; Gürses, A.; Ejder, M.; Açikyildiz, M. Adsorptive removal of phosphate from aqueous solutions using raw and calcinated dolomite. *J. Hazard. Mater.* **2006**, *128*, 273–279. [CrossRef]
15. Li, J.; Cao, L.; Li, B.; Huang, H.; Yu, W.; Sun, C.; Long, K.; Young, B. Utilization of activated sludge and shell wastes for the preparation of Ca-loaded biochar for phosphate removal and recovery. *J. Clean. Prod.* **2023**, *382*, 135395. [CrossRef]
16. Xiong, J.; Qin, Y.; Islam, E.; Yue, M.; Wang, W. Phosphate removal from solution using powdered freshwater mussel shells. *Desalination* **2011**, *276*, 317–321. [CrossRef]
17. Song, X.; Pan, Y.; Wu, Q.; Cheng, Z.; Ma, W. Phosphate removal from aqueous solutions by adsorption using ferric sludge. *Desalination* **2011**, *280*, 384–390. [CrossRef]
18. Yang, S.; Zhao, Y.; Chen, R.; Feng, C.; Zhang, Z.; Lei, Z.; Yang, Y. A novel tablet porous material developed as adsorbent for phosphate removal and recycling. *J. Colloid Interface Sci.* **2013**, *396*, 197–204. [CrossRef]
19. Du, M.; Zhang, Y.; Wang, Z.; Lv, M.; Tang, A.; Yu, Y.; Qu, X.; Chen, Z.; Wen, Q.; Li, A. Insight into the synthesis and adsorption mechanism of adsorbents for efficient phosphate removal: Exploration from synthesis to modification. *Chem. Eng. J.* **2022**, *442*, 136147. [CrossRef]
20. Aouan, B.; Alehyen, S.; Fadil, M.; El Alouani, M.; Saufi, H.; El Herradi, E.H.; El Makhoukhi, F.; Taibi, M. Development and optimization of geopolymer adsorbent for water treatment: Application of mixture design approach. *J. Environ. Manag.* **2023**, *338*, 117853. [CrossRef] [PubMed]
21. El Alouani, M.; Alehyen, S.; Aouan, B.; Mabrouki, J.; Saufi, H. Application of mesoporous fly ash as a low-cost adsorbent for effective removal and immobilization of hazardous pollutants in aqueous environments. *Model. Earth Syst. Environ.* **2023**, *9*, 3539–3552. [CrossRef]
22. Siyal, A.A.; Shamsuddin, M.R.; Khahro, S.H.; Low, A.; Ayoub, M. Optimization of synthesis of geopolymer adsorbent for the effective removal of anionic surfactant from aqueous solution. *J. Environ. Chem. Eng.* **2021**, *9*, 104949. [CrossRef]
23. Cheng, T.W.; Lee, M.L.; Ko, M.S.; Ueng, T.H.; Yang, S.F. The heavy metal adsorption characteristics on metakaolin-based geopolymer. *Appl. Clay Sci.* **2012**, *56*, 90–96. [CrossRef]
24. Cong, P.; Cheng, Y. Advances in geopolymer materials: A comprehensive review. *J. Traffic Transp. Eng. (Engl. Ed.)* **2021**, *8*, 283–314. [CrossRef]
25. Bilal, M.; Ihsanullah, I.; Younas, M.; Ul Hassan Shah, M. Recent advances in applications of low-cost adsorbents for the removal of heavy metals from water: A critical review. *Sep. Purif. Technol.* **2021**, *278*, 119510. [CrossRef]
26. Jo, M.; Soto, L.; Arocho, M.; St John, J.; Hwang, S. Optimum mix design of fly ash geopolymer paste and its use in pervious concrete for removal of fecal coliforms and phosphorus in water. *Constr. Build. Mater.* **2015**, *93*, 1097–1104. [CrossRef]
27. De Rossi, A.; Simão, L.; Ribeiro, M.J.; Novais, R.M.; Labrincha, J.A.; Hotza, D.; Moreira, R.F.P.M. In-situ synthesis of zeolites by geopolymerization of biomass fly ash and metakaolin. *Mater. Lett.* **2019**, *236*, 644–648. [CrossRef]
28. Duan, P.; Yan, C.; Zhou, W. Influence of partial replacement of fly ash by metakaolin on mechanical properties and microstructure of fly ash geopolymer paste exposed to sulfate attack. *Ceram. Int.* **2016**, *42*, 3504–3517. [CrossRef]
29. Abdulkareem, O.A.; Ramli, M.; Matthews, J.C. Production of geopolymer mortar system containing high calcium biomass wood ash as a partial substitution to fly ash: An early age evaluation. *Compos. Part B Eng.* **2019**, *174*, 106941. [CrossRef]
30. Ardhira, P.J.; Shukla, S.K.; Sathyan, D. Synthesis of geopolymer mortar from biomass ashes and forecasting its compressive strength behaviour. *Case Stud. Constr. Mater.* **2024**, *21*, e03581. [CrossRef]

31. Rosmayanti, I.; Maryani, E.; Samadhi, T.W. Preparation of porous geopolymer from biomass ash for synthetic dye adsorbent. *AIP Conf. Proc.* **2024**, *3071*, 020018. [CrossRef]
32. Chen, J.; Huang, R.; Ouyang, H.; Yu, G.; Liang, Y.; Zheng, Q. Utilization of dredged river sediments to synthesize zeolite for Cd(II) removal from wastewater. *J. Clean. Prod.* **2021**, *320*, 128861. [CrossRef]
33. Gonçalves, N.P.F.; Olhero, S.M.; Labrincha, J.A.; Novais, R.M. 3D-printed red mud/metakaolin-based geopolymers as water pollutant sorbents of methylene blue. *J. Clean. Prod.* **2023**, *383*, 135315. [CrossRef]
34. Zhang, B.; Yu, T.; Deng, L.; Li, Y.; Guo, H.; Zhou, J.; Li, L.; Peng, Y. Ion-adsorption type rare earth tailings for preparation of alkali-based geopolymer with capacity for heavy metals immobilization. *Cem. Concr. Compos.* **2022**, *134*, 104768. [CrossRef]
35. Watanabe, Y.; Kobayashi, T. Geopolymers Prepared by Microwave Treatments. In *Advanced Ceramics. Advances in Material Research and Technology*; Springer: Cham, Switzerland, 2024; pp. 259–280. [CrossRef]
36. Bai, C.; Colombo, P. High-porosity geopolymer membrane supports by peroxide route with the addition of egg white as surfactant. *Ceram. Int.* **2017**, *43*, 2267–2273. [CrossRef]
37. Bai, C.; Colombo, P. Processing, properties and applications of highly porous geopolymers: A review. *Ceram. Int.* **2018**, *44*, 16103–16118. [CrossRef]
38. Bai, C.; Zheng, K.; Sun, F.; Wang, X.; Zhang, L.; Zheng, T.; Colombo, P.; Wang, B. A review on metakaolin-based porous geopolymers. *Appl. Clay Sci.* **2024**, *258*, 107490. [CrossRef]
39. Reeb, C.; Pierlot, C.; Davy, C.; Lambertin, D. Incorporation of organic liquids into geopolymer materials—A review of processing, properties and applications. *Ceram. Int.* **2021**, *47*, 7369–7385. [CrossRef]
40. Khale, D.; Chaudhary, R. Mechanism of geopolymerization and factors influencing its development: A review. *J. Mater. Sci.* **2007**, *42*, 729–746. [CrossRef]
41. Kočí, V.; Černý, R. Directly foamed geopolymers: A review of recent studies. *Cem. Concr. Compos.* **2022**, *130*, 104530. [CrossRef]
42. Zhang, X.; Zhang, X.; Li, X.; Tian, D.; Ma, M.; Wang, T. Optimized pore structure and high permeability of metakaolin/fly-ash-based geopolymer foams from Al– and H_2O_2–sodium oleate foaming systems. *Ceram. Int.* **2022**, *48*, 18348–18360. [CrossRef]
43. Ducman, V.; Korat, L. Characterization of geopolymer fly-ash based foams obtained with the addition of Al powder or H2O2 as foaming agents. *Mater. Charact.* **2016**, *113*, 207–213. [CrossRef]
44. Hajimohammadi, A.; Ngo, T.; Mendis, P.; Sanjayan, J. Regulating the chemical foaming reaction to control the porosity of geopolymer foams. *Mater. Des.* **2017**, *120*, 255–265. [CrossRef]
45. Landi, E.; Medri, V.; Papa, E.; Dedecek, J.; Klein, P.; Benito, P.; Vaccari, A. Alkali-bonded ceramics with hierarchical tailored porosity. *Appl. Clay Sci.* **2013**, *73*, 56–64. [CrossRef]
46. Kränzlein, E.; Pöllmann, H.; Krcmar, W. Metal powders as foaming agents in fly ash based geopolymer synthesis and their impact on the structure depending on the Na/Al ratio. *Cem. Concr. Compos.* **2018**, *90*, 161–168. [CrossRef]
47. Kioupis, D.; Zisimopoulou, A.; Tsivilis, S.; Kakali, G. Development of porous geopolymers foamed by aluminum and zinc powders. *Ceram. Int.* **2021**, *47*, 26280–26292. [CrossRef]
48. Phavongkham, V.; Wattanasiriwech, S.; Cheng, T.W.; Wattanasiriwech, D. Effects of surfactant on thermo-mechanical behavior of geopolymer foam paste made with sodium perborate foaming agent. *Constr. Build. Mater.* **2020**, *243*, 118282. [CrossRef]
49. Karmil, F.Z.; Mountadar, S.; El Alaoui-Belghiti, H.; Majid, F.; Rich, A.; Mountadar, M. Desalination RO reject brine as a novel-based porous geopolymer for phosphorus removal from contaminated media. *Chemosphere* **2024**, *358*, 142202. [CrossRef]
50. Zhang, X.; Bai, C.; Qiao, Y.; Wang, X.; Jia, D.; Li, H.; Colombo, P. Porous geopolymer composites: A review. *Compos. Part A Appl. Sci. Manuf.* **2021**, *150*, 106629. [CrossRef]
51. Chen, X.; Guo, Y.; Ding, S.; Zhang, H.; Xia, F.; Wang, J.; Zhou, M. Utilization of red mud in geopolymer-based pervious concrete with function of adsorption of heavy metal ions. *J. Clean. Prod.* **2019**, *207*, 789–800. [CrossRef]
52. Luukkonen, T.; Runtti, H.; Niskanen, M.; Tolonen, E.T.; Sarkkinen, M.; Kemppainen, K.; Rämö, J.; Lassi, U. Simultaneous removal of Ni(II), As(III), and Sb(III) from spiked mine effluent with metakaolin and blast-furnace-slag geopolymers. *J. Environ. Manag.* **2016**, *166*, 579–588. [CrossRef]
53. Bouna, L.; Ait El Fakir, A.; Benlhachemi, A.; Draoui, K.; Ezahri, M.; Bakiz, B.; Villain, S.; Guinneton, F.; Elalem, N. Synthesis and characterization of mesoporous geopolymer based on Moroccan kaolinite rich clay. *Appl. Clay Sci.* **2020**, *196*, 105764. [CrossRef]
54. Karunanithi, R.; Szogi, A.A.; Bolan, N.; Naidu, R.; Loganathan, P.; Hunt, P.G.; Vanotti, M.B.; Saint, C.P.; Ok, Y.S.; Krishnamoorthy, S. Phosphorus Recovery and Reuse from Waste Streams. *Adv. Agron.* **2015**, *131*, 173–250. [CrossRef]
55. Fang, H.; Cui, Z.; He, G.; Huang, L.; Chen, M. Phosphorus adsorption onto clay minerals and iron oxide with consideration of heterogeneous particle morphology. *Sci. Total Environ.* **2017**, *605–606*, 357–367. [CrossRef]
56. Guan, W.; Ji, F.; Chen, Q.; Yan, P.; Zhang, Q. Preparation and phosphorus recovery performance of porous calcium–silicate–hydrate. *Ceram. Int.* **2013**, *39*, 1385–1391. [CrossRef]
57. Bus, A. Assessment of sorption properties and kinetic reaction of phosphorus reactive material to limit diffuse pollution. *Ann. Warsaw Univ. Life Sci.—SGGW Land Reclam.* **2017**, *49*, 143–152. [CrossRef]

58. Renman, A.; Renman, G. Long-term phosphate removal by the calcium-silicate material Polonite in wastewater filtration systems. *Chemosphere* **2010**, *79*, 659–664. [CrossRef] [PubMed]
59. Li, X.G.; Liu, Z.L.; Lv, Y.; Cai, L.X.; Jiang, D.B.; Jiang, W.G.; Jian, S. Utilization of municipal solid waste incineration bottom ash in autoclaved aerated concrete. *Constr. Build. Mater.* **2018**, *178*, 175–182. [CrossRef]
60. Yu, X.G.; Luo, S.S.; Gao, Y.N.; Wang, H.F.; Li, Y.X.; Wei, Y.R.; Wang, X.J. Pore Structure and Microstructure of Foam Concrete. *Adv. Mater. Res.* **2011**, *177*, 530–532. [CrossRef]
61. Elsener, B.; Angst, U. *Science and Technology of Concrete Admixtures*, 1st ed.; Elsevier: Amsterdam, The Netherlands, 2016.
62. *EN ISO 10523:2012*; Water Quality—Determination of pH. European Committee for Standardization: Brussels, Belgium, 2012.
63. *EN 1899-2:1998*; Water Quality—Determination of Biochemical Oxygen Demand After n Days (BODn)—Part 2: Method for Undiluted Samples. European Committee for Standardization: Brussels, Belgium, 2000.
64. *EN 872:2005*; Water Quality—Determination of Suspended Solids—Method by Filtration Through Glass Fibre Filters. European Committee for Standardization: Brussels, Belgium, 2005.
65. *EN 26777:1999*; Water Quality—Determination of Nitrite—Molecular Absorption Spectrometric Method. European Committee for Standardization: Brussels, Belgium, 1999.
66. *EN 25663:2000*; Water Quality—Determination of Kjeldahl Nitrogen—Method After Mineralization with Selenium. European Committee for Standardization: Brussels, Belgium, 2000.
67. *EN ISO 7150-1:1994*; Water Quality—Determination of Ammonium. Part 1: Manual Spectrometric Method. European Committee for Standardization: Brussels, Belgium, 1994.
68. *EN ISO 7890-3:1998*; Water Quality—Determination of Nitrate. Part 3: Spectrometric Method Using Sulfosalicylic Acid. European Committee for Standardization: Brussels, Belgium, 1998.
69. *EN ISO 6878:2004*; Water Quality—Determination of Phosphorus—Ammonium Molybdate Spectrometric Method. European Committee for Standardization: Brussels, Belgium, 2004.
70. *EN 678:2000*; Determination of the Dry Density of Autoclaved Aerated Concrete. European Committee for Standardization: Brussels, Belgium, 2000.
71. *LST EN 679:2005*; Determination of the Compressive Strength of Autoclaved Aerated Concrete. European Committee for Standardization: Brussels, Belgium, 2005.
72. Keriene, J.; Kligys, M.; Laukaitis, A.; Yakovlev, G.; Špokauskas, A.; Aleknevičius, M. The influence of multi-walled carbon nanotubes additive on properties of non-autoclaved and autoclaved aerated concretes. *Constr. Build. Mater.* **2013**, *49*, 527–535. [CrossRef]
73. Schober, G. Porosity in autoclaved aerated concrete (AAC): A review on pore structure, types of porosity, measurement methods and effects of porosity on properties. *Cem. Wapno Beton* **2011**, *2011*, 39–43.
74. Nguyen Trong, L.; Asamoto, S.; Matsui, K. Sorption isotherm and length change behavior of autoclaved aerated concrete. *Cem. Concr. Compos.* **2018**, *94*, 136–144. [CrossRef]
75. Matsui, K.; Kikuma, J.; Tsunashima, M.; Ishikawa, T.; Matsuno, S.Y.; Ogawa, A.; Sato, M. In situ time-resolved X-ray diffraction of tobermorite formation in autoclaved aerated concrete: Influence of silica source reactivity and Al addition. *Cem. Concr. Res.* **2011**, *41*, 510–519. [CrossRef]
76. Salih, M.A.; Farzadnia, N.; Abang Ali, A.A.; Demirboga, R. Effect of different curing temperatures on alkali activated palm oil fuel ash paste. *Constr. Build. Mater.* **2015**, *94*, 116–125. [CrossRef]
77. Zhu, C.; Pranckevičienė, J.; Pundienė, I.; Kizinievič, O. Utilising Phosphogypsum and Biomass Fly Ash By-Products in Alkali-Activated Materials. *Sustainability* **2024**, *16*, 1084. [CrossRef]
78. Pundienė, I.; Pranckevičienė, J.; Zhu, C.; Kligys, M. The role of temperature and activator solution molarity on the viscosity and hard structure formation of geopolymer pastes. *Constr. Build. Mater.* **2021**, *272*, 121661. [CrossRef]
79. Okada, K.; Ooyama, A.; Isobe, T.; Kameshima, Y.; Nakajima, A.; MacKenzie, K.J.D. Water retention properties of porous geopolymers for use in cooling applications. *J. Eur. Ceram. Soc.* **2009**, *29*, 1917–1923. [CrossRef]
80. Jiang, J.; Yang, Y.; Hou, L.; Lu, Z.; Li, J.; Niu, Y. Facile preparation and hardened properties of porous geopolymer-supported zeolite based on swelled bentonite. *Constr. Build. Mater.* **2019**, *228*, 117040. [CrossRef]
81. Ettahiri, Y.; Bouargane, B.; Fritah, K.; Akhsassi, B.; Pérez-Villarejo, L.; Aziz, A.; Bouna, L.; Benlhachemi, A.; Novais, R.M. A state-of-the-art review of recent advances in porous geopolymer: Applications in adsorption of inorganic and organic contaminants in water. *Constr. Build. Mater.* **2023**, *395*, 132269. [CrossRef]
82. Huang, X.Y.; Ni, W.; Cui, W.H.; Wang, Z.J.; Zhu, L.P. Preparation of autoclaved aerated concrete using copper tailings and blast furnace slag. *Constr. Build. Mater.* **2012**, *27*, 1–5. [CrossRef]
83. Song, Y.; Li, B.; Yang, E.H.; Liu, Y.; Ding, T. Feasibility study on utilization of municipal solid waste incineration bottom ash as aerating agent for the production of autoclaved aerated concrete. *Cem. Concr. Compos.* **2015**, *56*, 51–58. [CrossRef]
84. Jaya, N.A.; Yun-Ming, L.; Cheng-Yong, H.; Abdullah, M.M.A.B.; Hussin, K. Correlation between pore structure, compressive strength and thermal conductivity of porous metakaolin geopolymer. *Constr. Build. Mater.* **2020**, *247*, 118641. [CrossRef]

85. Guo, X.; Yu, H.; Yao, H.; Lin, F.; Salama, E.; Ossman, M.; Yan, B.; Chen, G. Green transformation of oily sludge through geopolymer: Material properties and hydration mechanisms. *Chemosphere* **2024**, *364*, 143132. [CrossRef]
86. Shi, J.; Li, H.; Shen, Y. Effects of nano-calcium carbonate on the durability and mechanisms of sludge-based geopolymer. *Constr. Build. Mater.* **2025**, *503*, 144518. [CrossRef]
87. Kurama, H.; Topçu, I.B.; Karakurt, C. Properties of the autoclaved aerated concrete produced from coal bottom ash. *J. Mater. Process. Technol.* **2009**, *209*, 767–773. [CrossRef]
88. Kunchariyakun, K.; Asavapisit, S.; Sombatsompop, K. Properties of autoclaved aerated concrete incorporating rice husk ash as partial replacement for fine aggregate. *Cem. Concr. Compos.* **2015**, *55*, 11–16. [CrossRef]
89. Al-mashhadani, M.M.; Canpolat, O. Effect of various NaOH molarities and various filling materials on the behavior of fly ash based geopolymer composites. *Constr. Build. Mater.* **2020**, *262*, 120560. [CrossRef]
90. Wongpaun, A.; Tangchirapat, W.; Suwan, T.; Fan, M. Factors affecting compressive strength and expansion due to alkali-silica reaction of fly ash-based alkaline activated mortar. *Case Stud. Constr. Mater.* **2023**, *19*, e02595. [CrossRef]
91. Mohamed, O.A.; Najm, O.; Zuaiter, H.A.; Saleem, S.K.; Ivak, S.; Al-Aribe, K. Effect of activator concentration on setting time, workability and compressive strength of sustainable concrete with alkali-activated slag binder. *Mater. Today Proc.* 2024; *in press*. [CrossRef]
92. Wang, H.; Wu, H.; Xing, Z.; Wang, R.; Dai, S.; Wang, H.; Wu, H.; Xing, Z.; Wang, R.; Dai, S. The Effect of Various Si/Al, Na/Al Molar Ratios and Free Water on Micromorphology and Macro-Strength of Metakaolin-Based Geopolymer. *Materials* **2021**, *14*, 3845. [CrossRef]
93. Kubba, Z.; Fahim Huseien, G.; Sam, A.R.M.; Shah, K.W.; Asaad, M.A.; Ismail, M.; Tahir, M.M.; Mirza, J. Impact of curing temperatures and alkaline activators on compressive strength and porosity of ternary blended geopolymer mortars. *Case Stud. Constr. Mater.* **2018**, *9*, e00205. [CrossRef]
94. L'Hôpital, E.; Lothenbach, B.; Le Saout, G.; Kulik, D.; Scrivener, K. Incorporation of aluminium in calcium-silicate-hydrates. *Cem. Concr. Res.* **2015**, *75*, 91–103. [CrossRef]
95. Ishwarya, G.; Singh, B.; Deshwal, S.; Bhattacharyya, S.K. Effect of sodium carbonate/sodium silicate activator on the rheology, geopolymerization and strength of fly ash/slag geopolymer pastes. *Cem. Concr. Compos.* **2019**, *97*, 226–238. [CrossRef]
96. Hardjito, D.; Cheak, C.C.; Lee Ing, C.H. Strength and Setting Times of Low Calcium Fly Ash-based Geopolymer Mortar. *Mod. Appl. Sci.* **2008**, *2*, p3. [CrossRef]
97. Luhar, S.; Cheng, T.W.; Nicolaides, D.; Luhar, I.; Panias, D.; Sakkas, K. Valorisation of glass wastes for the development of geopolymer composites—Durability, thermal and microstructural properties: A review. *Constr. Build. Mater.* **2019**, *222*, 673–687. [CrossRef]
98. Wang, Y.; Li, P.; Li, L.; Liu, J.; Zheng, T. The phosphorus removal by dewatered-sludge-based flocculants during municipal wastewater treatment process: Parameter optimization and kinetic modelling of adsorption. *J. Water Process Eng.* **2025**, *78*, 108697. [CrossRef]
99. Park, J.-H.; Hwang, S.-W.; Lee, S.-L.; Lee, J.-H.; Seo, D.-C. Sorption behavior of phosphate by fly ash discharged from biomass thermal power plant. *Appl. Biol. Chem.* **2021**, *64*, 43. [CrossRef]
100. Park, J.H.; Eom, J.H.; Lee, S.L.; Hwang, S.W.; Kim, S.H.; Kang, S.W.; Yun, J.J.; Cho, J.S.; Lee, Y.H.; Seo, D.C. Exploration of the potential capacity of fly ash and bottom ash derived from wood pellet-based thermal power plant for heavy metal removal. *Sci. Total Environ.* **2020**, *740*, 140205. [CrossRef]
101. Miculescu, F.; Luță, C.; Constantinescu, A.E.; Maidaniuc, A.; Mocanu, A.C.; Miculescu, M.; Voicu, Ș.I.; Ciocan, L.T. Considerations and Influencing Parameters in EDS Microanalysis of Biogenic Hydroxyapatite. *J. Funct. Biomater.* **2020**, *11*, 82. [CrossRef] [PubMed]
102. Zhang, K.; Van Dyk, L.; He, D.; Deng, J.; Liu, S.; Zhao, H. Synthesis of zeolite from fly ash and its adsorption of phosphorus in wastewater. *Green Process. Synth.* **2021**, *10*, 349–360. [CrossRef]
103. Mažeikienė, A.; Vaiškūnaitė, R.; Šarko, J. Sand from groundwater treatment coated with iron and manganese used for phosphorus removal from wastewater. *Sci. Total Environ.* **2021**, *764*, 142915. [CrossRef]
104. Salam, M.A.; Mokhtar, M.; Albukhari, S.M.; Baamer, D.F.; Palmisano, L.; AlHammadi, A.A.; Abukhadra, M.R. Synthesis of zeolite/geopolymer composite for enhanced sequestration of phosphate (PO_4^{3-}) and ammonium (NH_4^+) ions; equilibrium properties and realistic study. *J. Environ. Manag.* **2021**, *300*, 113723. [CrossRef] [PubMed]
105. Stepova, K.; Fediv, I.; Mažeikienė, A.; Šarko, J.; Mažeika, J. Adsorption of Ammonium Ions and Phosphates on Natural and Modified Clinoptilolite: Isotherm and Breakthrough Curve Measurements. *Water* **2023**, *15*, 1933. [CrossRef]
106. Nujić, M.; Milinković, D.; Habuda-Stanić, M. Nitrate removal from water by ion exchange. *Croat. J. Food Sci. Technol.* **2017**, *9*, 182–186. [CrossRef]
107. Chen, Y.; Zhang, C.; Chen, Z.; Deng, Z.; Wang, Q.; Zou, Q.; Li, J.; Zhang, Y.; Wang, X. Achieving nitrite shunt using in-situ free ammonia enriched by natural zeolite: Pilot-scale mainstream anammox with flexible nitritation strategy. *Water Res.* **2024**, *265*, 122314. [CrossRef] [PubMed]

108. Zhao, Q.; Zhang, L.; Li, J.; Jia, T.; Deng, L.; Liu, Q.; Sui, J.; Zhang, Q.; Peng, Y. Carbon-Restricted Anoxic Zone as an Overlooked Anammox Hotspot in Municipal Wastewater Treatment Plants. *Environ. Sci. Technol.* **2023**, *57*, 21767–21778. [CrossRef]
109. Jiang, Y.; Yang, X.; Zeng, D.; Su, Y.; Zhang, Y. Nitrate recovery from groundwater and simultaneous upcycling into single-cell protein using a novel hybrid biological-inorganic system. *Water Res.* **2024**, *263*, 122127. [CrossRef]
110. Wang, R.; Zhou, X.; Zhang, W.; Ye, J.; Wang, J. Transport mechanism of uranyl nitrate in nanopore of geopolymer with different Si/Al ratios: Molecular dynamics simulation. *J. Solid State Chem.* **2024**, *331*, 124542. [CrossRef]
111. Mosca, A.; Öhrman, O.; Hedlund, J.; Perdana, I.; Creaser, D. NO_2 and N_2 sorption in MFI films with varying Si/Al and Na/Al ratios. *Microporous Mesoporous Mater.* **2009**, *120*, 195–205. [CrossRef]
112. Hou, C.; Wu, H.; Zhou, Z.; Peng, S.; Wu, K.; Wang, Y.; Xu, L.; Chen, Z.; Lei, Z.; Wu, D. Enhancing selective NH4+ recovery from wastewater using modified zeolite-based flow electrode capacitive deionization. *Water Res.* **2025**, *268*, 122589. [CrossRef] [PubMed]
113. You, X.; Liu, S.; Dai, C.; Zhong, G.; Duan, Y.; Guo, Y.; Makhinov, A.N.; Júnior, J.T.A.; Tu, Y.; Leong, K.H. Effects of EDTA on adsorption of Cd(II) and Pb(II) by soil minerals in low-permeability layers: Batch experiments and microscopic characterization. *Environ. Sci. Pollut. Res.* **2020**, *27*, 41623–41638. [CrossRef]
114. Eshraghi, F.; Nezamzadeh-Ejhieh, A. EDTA-functionalized clinoptilolite nanoparticles as an effective adsorbent for Pb(II) removal. *Environ. Sci. Pollut. Res.* **2018**, *25*, 14043–14056. [CrossRef] [PubMed]
115. Cardoso, A.M.; Paprocki, A.; Ferret, L.S.; Azevedo, C.M.N.; Pires, M. Synthesis of zeolite Na-P1 under mild conditions using Brazilian coal fly ash and its application in wastewater treatment. *Fuel* **2015**, *139*, 59–67. [CrossRef]
116. Zheng, Z.; Ma, X.; Zhang, Z.; Li, Y. In-situ transition of amorphous gels to Na-P1 zeolite in geopolymer: Mechanical and adsorption properties. *Constr. Build. Mater.* **2019**, *202*, 851–860. [CrossRef]
117. Elfadaly, E.; Othman, A.M.; Aly, M.H.; Elgarhy, W.A.; Abdellatief, M. Assessing performance and environmental benefits of high-performance geopolymer mortar incorporating pumice and rice straw ash. *Sustain. Chem. Pharm.* **2025**, *44*, 101918. [CrossRef]
118. Van Deventer, J.S.J. Progress in the Adoption of Geopolymer Cement. In *Handbook of Low Carbon Concrete*; Elsevier Inc.: Amsterdam, The Netherlands, 2016; pp. 217–262. [CrossRef]
119. Agashua, L.O.; Arum, C.; Oluyemi-Ayibiowu, B.D.; Ikumapayi, C.M. A systematic review of geopolymer materials: Innovations, prevailing constraints and resolutions. *Sinergi* **2024**, *28*, 473–488. [CrossRef]
120. Kadhim, A.; Mankhi, B.S.; Al-Bujasim, M. Review of Geopolymer Technology, Barriers and Limitations. *Al-Mustaqbal J. Sustain. Eng. Sci.* **2024**, *2*, 4. [CrossRef]
121. Renu; Sithole, T. A review on regeneration of adsorbent and recovery of metals: Adsorbent disposal and regeneration mechanism. *S. Afr. J. Chem. Eng.* **2024**, *50*, 39–50. [CrossRef]